Published November 3, 2016

Plastin 1 widens stereocilia by transforming actin filament packing from hexagonal to liquid

Jocelyn F. Krey,[1,2] Evan S. Krystofiak,[4] Rachel A. Dumont,[1,2] Sarath Vijayakumar,[5] Dongseok Choi,[3,6] Francisco Rivero,[7] Bechara Kachar,[4] Sherri M. Jones,[5] and Peter G. Barr-Gillespie[1,2]

[1]Oregon Hearing Research Center, [2]Vollum Institute, and [3]Oregon Health and Science University–Portland State University School of Public Health, Oregon Health and Science University, Portland, OR 97239
[4]Laboratory of Cell Structure and Dynamics, National Institute on Deafness and Other Communication Disorders, National Institutes of Health, Bethesda, MD 20892
[5]Department of Special Education and Communication Disorders, University of Nebraska-Lincoln, Lincoln, NE 68583
[6]Graduate School of Dentistry, Kyung Hee University, Seoul 02447, Republic of Korea
[7]Centre for Cardiovascular and Metabolic Research, The Hull York Medical School, University of Hull, Hull HU6 7RX, England, UK

With their essential role in inner ear function, stereocilia of sensory hair cells demonstrate the importance of cellular actin protrusions. Actin packing in stereocilia is mediated by cross-linkers of the plastin, fascin, and espin families. Although mice lacking espin (ESPN) have no vestibular or auditory function, we found that mice that either lacked plastin 1 (PLS1) or had nonfunctional fascin 2 (FSCN2) had reduced inner ear function, with double-mutant mice most strongly affected. Targeted mass spectrometry indicated that PLS1 was the most abundant cross-linker in vestibular stereocilia and the second most abundant protein overall; ESPN only accounted for ∼15% of the total cross-linkers in bundles. Mouse utricle stereocilia lacking PLS1 were shorter and thinner than wild-type stereocilia. Surprisingly, although wild-type stereocilia had random liquid packing of their actin filaments, stereocilia lacking PLS1 had orderly hexagonal packing. Although all three cross-linkers are required for stereocilia structure and function, PLS1 biases actin toward liquid packing, which allows stereocilia to grow to a greater diameter.

Introduction

Organized arrays of actin filaments play fundamental roles in all eukaryotic cells, which construct at least 15 different types of actin arrays using distinct sets of actin-binding proteins (Chhabra and Higgs, 2007; Michelot and Drubin, 2011). A special subset of these arrays comprises membrane-enveloped protrusions of tightly bundled parallel actin filaments, which include filopodia, microvilli, and inner ear stereocilia. These protrusions enhance cells' abilities to transduce extracellular signals and transport essential metabolites (Gupton and Gertler, 2007; Crawley et al., 2014).

Stereocilia of the inner ear's sensory hair cells are particularly exaggerated examples of actin protrusions. Dozens to hundreds of coupled stereocilia make up the hair bundle, the organelle in the inner ear that transduces sound or head movements into electrical signals (Fig. 1 A). Each stereocilium is filled with a paracrystalline array of parallel actin filaments; an interfilament distance of ∼10 nm (Tilney et al., 1980) indicates that cross-linking is performed by tight actin cross-linkers, which include the espin, fascin, and plastin families (Volkmann et al., 2001; Purdy et al., 2007; Jansen et al., 2011). Indeed, fascin 2 (FSCN2), plastin 1 (PLS1), and espin (ESPN) have each been reported to be abundant in hair cells (Tilney et al., 1989; Zheng et al., 2000; Shin et al., 2010; Fig. 1 B). Bundled, parallel actin filaments in biological structures are packed either hexagonally or with liquid order, where the filaments show a high degree of order without being arranged on a regular lattice (Tilney et al., 1980). Stereocilia actin packing is either hexagonal, as seen in chick cochlea and utricle (Tilney et al., 1983; Shin et al., 2013), or liquid, as seen in mouse inner hair cells (IHCs) and lizard cochlea (DeRosier et al., 1980; Tilney et al., 1980; Mogensen et al., 2007).

Because they rely on stereocilia for their physiological function, hair cells are ideal for studying structures made of bundled actin filaments. Hair-bundle phenotypes of human, mouse, and zebrafish mutants are often illuminating; mutations that inactivate hair cell function often do not affect other cell types, either because specialized paralogs are employed by hair cells or because compensation from related molecules can prevent loss of function in other cell types. In many cases, the morphological consequences of mutation of the genes encoding

Correspondence to Peter G. Barr-Gillespie: gillespp@ohsu.edu

Abbreviations used: ABR, auditory brainstem response; ANOVA, analysis of variance; DPOAE, distortion-product otoacoustic emission; eFASP, enhanced filter-aided sample preparation technique; FFT, fast Fourier transformation; IHC, inner hair cell; MS, mass spectrometry; MS/MS, tandem mass spectrometry; n1, negative peak 1; OHC, outer hair cell; p1, positive peak 1; SIM, structured illumination microscopy; SPL, sound-pressure level; VsEP, vestibular sensory-evoked potential.

The Rockefeller University Press $30.00
J. Cell Biol.
https://doi.org/10.1083/jcb.201606036

Published November 3, 2016

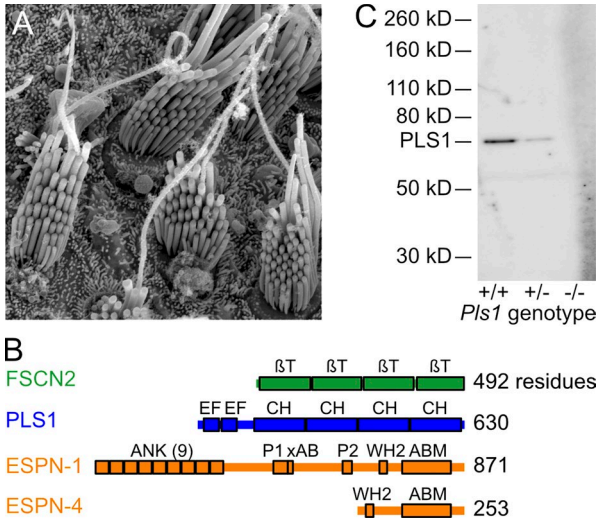

Figure 1. **Actin cross-linkers of mouse vestibular stereocilia.** (A) Scanning electron micrograph of P30 mouse utricle hair bundles. Panel full width is 15 µm. (B) Domain structure of the major stereocilia actin cross-linkers. FSCN2 (fascin 2) has four β-trefoil (βT) domains. PLS1 (plastin 1) has two EF-hands (EF) and four calponin homology (CH) domains. ESPN-1 (the longest espin splice form) has nine ankyrin repeats (ANK), two proline-rich domains (P1 and P2), a masked actin-binding domain (xAB) domain, a Wiskott-Aldrich homology 2 (WH2) domain, and an actin-binding module (ABM). ESPN-4 (the shortest espin splice form) just has WH2 and ABM domains. (C) Protein immunoblot showing PLS1 is absent in hair bundles isolated from *Pls1*$^{-/-}$ mice. Molecular mass markers (in kD) are indicated.

specific actin-binding proteins immediately suggest a function for that protein (Drummond et al., 2012).

Here, we examined stereocilia of the mouse vestibular system, which allowed us to combine phenotypic analysis of mice lacking functional versions of the cross-linkers with thorough protein quantitation and detailed structural analysis. Previous work showed that mutations in *Espn*, *Fscn2*, and *Pls1* all cause hearing loss, which manifests at different developmental ages for each mutant mouse (Zheng et al., 2000; Shin et al., 2010; Sekerková et al., 2011; Perrin et al., 2013; Taylor et al., 2015). Although *deaf jerker* mice (bearing a null mutation in *Espn*) lack balance function (Grüneberg et al., 1941; Jones et al., 2005), little is known about vestibular activity in mice lacking *Pls1* or *Fscn2*. We found that thresholds for vestibular evoked potentials, a measure of vestibular sensitivity, were significantly elevated in mice lacking functional PLS1, FSCN2, or both. Although PLS1 was the second most abundant protein of utricular bundles (considerably more abundant than FSCN2 and ESPN), bundles lacking PLS1 had unaltered levels of other cross-linkers. Utricle stereocilia from mice lacking PLS1 were significantly thinner and shorter than those of wild-type mice; by contrast, stereocilia from mice that express a nonfunctional form of FSCN2 had wild-type dimensions. Double-mutant stereocilia had dimensions that were similar to those mice only lacking PLS1. The mutants also varied markedly in their actin-filament packing. Although wild-type utricle stereocilia had liquid packing of their actin filaments, stereocilia formed without PLS1 had actin packed in a hexagonal lattice. Actin packing in utricle stereocilia with mutant FSCN2 was similar to that of wild type, but packing of actin filaments from double mutants was also hexagonal. These results show that PLS1 generates liquid packing of stereocilia actin, even though ESPN favors hexagonal packing. Finally, PLS1 is necessary for formation of stereocilia with larger diameters.

Results

Functional consequences of the absence of PLS1 or FSCN2 on auditory function

To better understand the role of PLS1 and FSCN2 in stereocilia function, we used *Pls1*$^{-/-}$ (Grimm-Günter et al., 2009; Revenu et al., 2012; Taylor et al., 2015) and B6.D2-*Fscn2*^{R109H} mice (Perrin et al., 2013); the latter line is referred to here as *Fscn2*^{R109H}. *Pls1*$^{-/-}$ mice were on a C57BL/6 background; we confirmed by protein immunoblotting (Fig. 1 C) and immunocytochemistry (Fig. S1, A–C) that PLS1 was absent from hair bundles in *Pls1*$^{-/-}$ mice and that heterozygotes had intermediate levels of PLS1 protein. *Fscn2*^{R109H} is a subcongenic strain containing mostly C57BL/6 except for the region surrounding the *Fscn2* gene, which was derived from the DBA2/J strain (Perrin et al., 2013). *Fscn2* is mutated in DBA2/J, and the R109H-FSCN2 protein produced in this strain can bind to actin filaments but cannot cross-link them (Perrin et al., 2013). Mice with this mutation in *Fscn2* exhibit progressive hearing loss (Shin et al., 2010). We used two strains of control mice, *Pls1*$^{+/+}$ and C57BL/6. As with *Pls1*$^{-/-}$ mice, *Pls1*$^{+/+}$ mice were derived from the original *Pls1* targeting experiments but were maintained as a separate inbred colony. With the exception of modest differences in auditory behavior, results were identical with the two control strains.

As previously reported (Taylor et al., 2015), *Pls1*$^{-/-}$ mice had substantially diminished hearing; thresholds for auditory brainstem responses (ABRs), which test the activity of the auditory system from external ear to brainstem, were significantly elevated in the 8- to 41-kHz frequency range when compared either to C57BL/6 mice or *Pls1*$^{+/+}$ littermates (Fig. 2 A). Likewise, *Fscn2*$^{R109H/R109H}$ mice had elevated ABR thresholds at high frequencies, similar to previous studies (Shin et al., 2010; Perrin et al., 2013). We also generated mice that both lacked PLS1 and had no functional FSCN2 (*Pls1*$^{-/-}$ *Fscn2*$^{R109H/R109H}$); these double mutant mice had a more severe hearing loss as judged by ABR threshold elevations (Fig. 2 A). Using Kruskal–Wallis nonparametric tests followed by Dunn's multiple comparison tests, we found that *Pls1*$^{+/+}$ ABR thresholds were not significantly different from those of C57BL/6 at all frequencies. In contrast, thresholds for *Pls1*$^{-/-}$ and *Pls1*$^{-/-}$ *Fscn2*$^{R109H/R109H}$ were significantly higher than C57BL/6 at all frequencies, whereas *Fscn2*$^{R109H/R109H}$ was significantly higher than C57BL/6 at only 32 and 41.2 kHz. Thus at 2 mo of age, loss of PLS1 causes hearing loss at all frequencies, whereas loss of FSCN2 only affects hearing at high frequencies.

At 8 kHz, where all mutant strains showed some ABR response, we also found that the positive peak 1 (p1) latencies were prolonged and p1 to negative peak 1 (n1) distance (p1-n1 amplitude) were decreased, with much larger effects for *Pls1*$^{-/-}$ and *Pls1*$^{-/-}$ *Fscn2*$^{R109H/R109H}$ mice (Fig. S2, A and C). When the responses were normalized for threshold, however, the latency-intensity and amplitude-intensity functions for mutant strains converged with those of control mice (Fig. S2, B and D), suggesting that sensitivity of the cochlea accounted for the differences, not features of the auditory nerve and brainstem.

Distortion-product otoacoustic emissions (DPOAEs), which test the activity of outer hair cells (OHCs), were smaller in all mutant strains compared with C57BL/6 mice, and the double-mutant mice were more affected than either single mutant alone (Fig. 2 B). Although all mutant strains showed DPOAE amplitudes at or near the noise floor for high frequencies (>27 kHz), lower frequencies (<27 kHz) showed some strain-specific distinctions. Note that as compared with C57BL/6, DPOAE

Published November 3, 2016

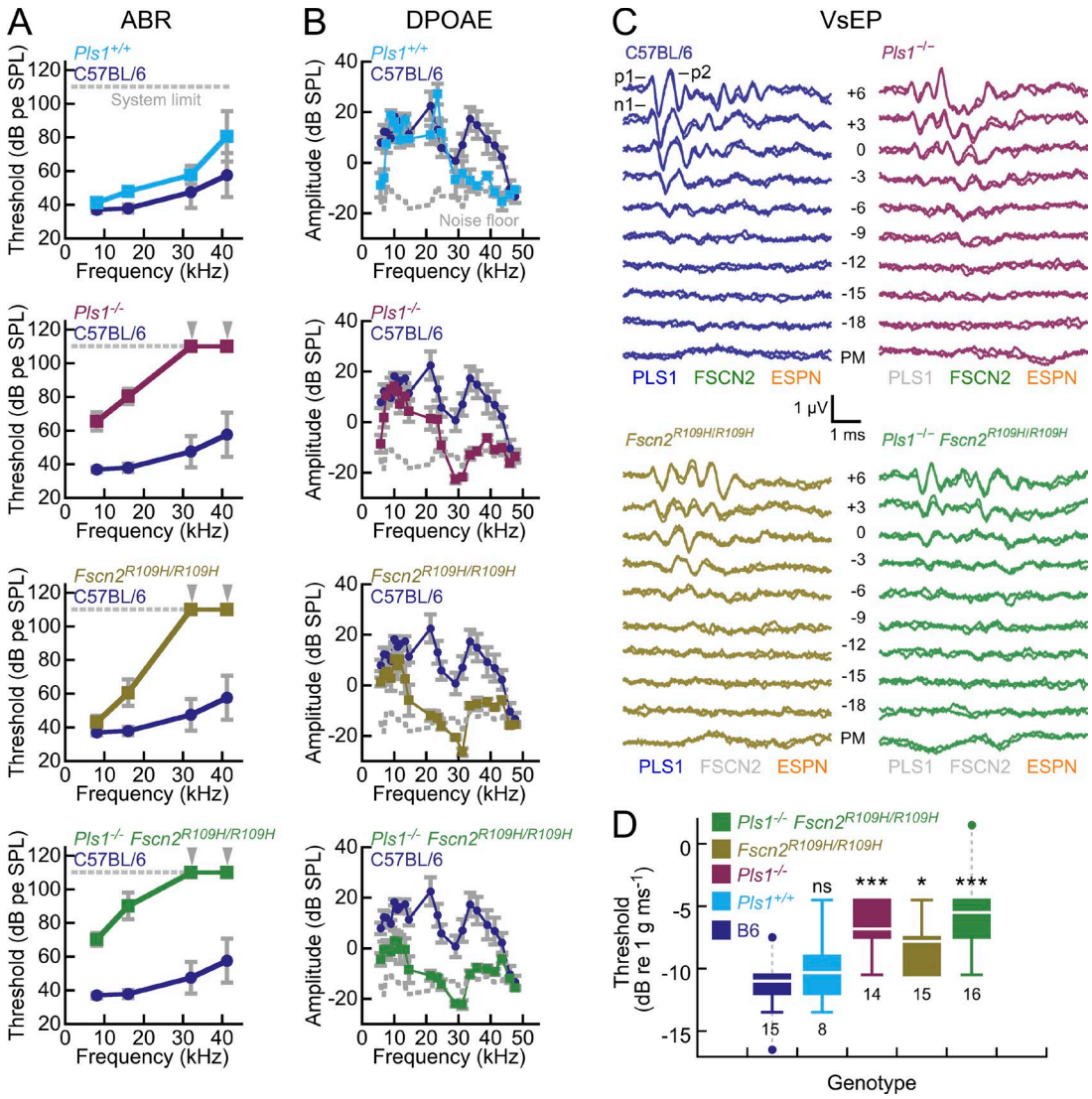

Figure 2. **Auditory and vestibular function is reduced in mice with mutations in *Pls1* and *Fscn2*.** (A) Auditory brainstem response (ABR) thresholds. dB pe SPL, decibel peak-equivalent sound-pressure level. For both ABRs and DPOAEs, the number of animals (2 mo old) tested were 8 C57BL/6, 6 *Pls1*$^{+/+}$, 11 *Pls1*$^{-/-}$, 7 *Fscn2*$^{R109H/R109H}$, and 10 *Pls1*$^{-/-}$ *Fscn2*$^{R109H/R109H}$. (B) Distortion-product otoacoustic emission (DPOAE) amplitudes. Frequency plotted is the geometric mean of f_1 and f_2. Dashed gray line represents the mean noise floor measured across all studies. (C) VsEP responses for stimuli of the indicated amplitudes (in decibels, referenced to 1 g/ms). Cross-linker symbols at the bottom of each panel indicate which proteins are functional (gray is nonfunctional or absent). p1, p2, and n1 of the VsEP response are indicated. (D) VsEP thresholds are mildly elevated in *Fscn2*$^{R109H/R109H}$ mice and moderately elevated in *Pls1*$^{-/-}$ and *Pls1*$^{-/-}$ *Fscn2*$^{R109H/R109H}$ mice (*, P < 0.05; ***, P < 0.001). In A and B, error bars indicate SD. In D, boxes indicate 25–75% range, white lines indicate mean, and solid colored bars indicate data range (except outliers, which are indicated by points and connected with gray dashed lines). Numbers of animals tested for each genotype are shown; all animals were 2 mo old.

amplitudes were diminished at high frequencies for *Pls1*$^{+/+}$ mice. At lower frequencies, DPOAE amplitudes for *Pls1*$^{-/-}$ mice were similar to those of C57BL/6 mice; however, *Fscn2*$^{R109H/R109H}$ ($P = 0.021$) and *Pls1*$^{-/-}$ *Fscn2*$^{R109H/R109H}$ ($P = 10^{-3}$) mice had significantly reduced amplitudes compared with C57BL/6 by analysis of variance (ANOVA). At higher frequencies, *Pls1*$^{-/-}$, *Fscn2*$^{R109H/R109H}$, and *Pls1*$^{-/-}$ *Fscn2*$^{R109H/R109H}$ were not significantly different from each other. Thus mice lacking FSCN2 had diminished DPOAEs across the frequencies tested, whereas those lacking PLS1 alone were only affected at high frequencies.

Functional consequences of the absence of PLS1 or FSCN2 on vestibular function

We assessed function of the vestibular system by measuring vestibular sensory-evoked potentials (VsEPs), compound action potentials generated by the vestibular portion of the eighth nerve and central relays (Jones and Jones, 1999; Jones et al., 2005, 2006) that arise in response to a linear jerk stimulus (Fig. 2, C and D). In particular, VsEP thresholds measure the sensitivity of the gravity receptor end organs, the utricle and the saccule. Although VsEPs have previously been used to show the profound functional deficits of mutations of the *Espn* gene (Jones et al., 2005), little is known of the significance of PLS1 and FSCN2 for the vestibular system.

Vestibular evoked potential thresholds were modestly elevated (sensitivity was decreased) in *Fscn2*$^{R109H/R109H}$ mice and more substantially elevated in *Pls1*$^{-/-}$ mice (Fig. 2 D). *Pls1*$^{-/-}$ *Fscn2*$^{R109H/R109H}$ mice were also strongly affected; they had VsEP thresholds that were only slightly elevated beyond *Pls1*$^{-/-}$ alone (Fig. 2 D). A multivariate ANOVA analysis re-

Published November 3, 2016

vealed statistical significance for *Fscn2*$^{R109H/R109H}$ mice (P = 0.013), compared with C57BL/6, and a much stronger effect for *Pls1*$^{-/-}$ and double-mutant mice (P < 10^{-3}). *Pls1*$^{+/+}$ VsEPs were not significantly different from those of C57BL/6 (P = 0.9). Latencies of the p1 and n1 waves were also significantly prolonged (P = 0.001); when normalized for threshold, however, the latency-intensity and amplitude-intensity functions essentially overlapped across genotypes (Fig. S3). The VsEP results thus indicate that loss of FSCN2 has a modest effect on vestibular function, and that loss of PLS1 more strongly elevates sensitivity thresholds. Nevertheless, even losing PLS1 and FSCN2 together has substantially less effect on vestibular function than does the loss of ESPN alone (Jones et al., 2005).

Accurate quantitation of actin cross-linkers in hair cells

An advantage of studying stereocilia cross-linkers in the vestibular system is the ability to isolate utricle hair bundles efficiently and quantify their proteins using mass spectrometry (MS; Krey et al., 2015). We previously estimated that the average chick utricle stereocilium has ∼400,000 actin monomers (Shin et al., 2013); our estimates based on the dimensions of bundles from mouse utricles (Li et al., 2008; Sekerková et al., 2011) ranged from ∼300,000 to ∼700,000 actin molecules per stereocilium, depending on assumptions used. To provide the greatest continuity with previous studies and to permit uniformity in comparisons of stoichiometry, we assumed that the average wild-type mouse utricle stereocilium also contains 400,000 actin monomers.

Although the stronger effects on vestibular function of *Espn* mutations than mutations of *Pls1* or *Fscn2* suggests that ESPN is the dominant actin cross-linker of stereocilia, a preliminary examination of cross-linker concentration in rat utricle stereocilia suggested that PLS1 and FSCN2 were present at much higher levels than ESPN (Shin et al., 2010). We used the twist-off bundle technique to isolate hair bundles from utricles of CD-1 mice (Gillespie and Hudspeth, 1991; Dumont et al., 2002; Krey et al., 2015), initially using in-gel digestion to prepare peptides (Shevchenko et al., 2006); we then performed quantitative shotgun MS with an Orbitrap instrument and MaxQuant analysis of the data (Cox and Mann, 2008; Cox et al., 2011). In experiments performed with bundles from postnatal day 4 (P4) to P6 ("P5") or P21 to P25 ("P23") mice (Krey et al., 2015), PLS1 was the second most abundant protein after actin; there were ∼30,000 PLS1 molecules per stereocilium (Fig. 3 A). FSCN2 was the second most abundant cross-linker, rising from ∼7,000 molecules per stereocilium at P5 to ∼19,000 at P23; ESPN was next but was only present at 3,500 (P5) and 1600 (P23) molecules per stereocilium. Corroborating the MS results, quantitative protein immunoblotting of cross-linkers in whole utricle extracts suggested that PLS1 was fourfold more abundant than FSCN2 (Fig. S4).

Although label-free quantitation using shotgun proteomics on average reports accurate protein concentrations, individual proteins can vary substantially in their signal per peptide. To accurately and precisely measure the abundances of actin, PLS1, FSCN2, ESPN (all isoforms), and ESPN-1, we used an Orbitrap Tribrid Fusion mass spectrometer to carry out targeted MS/MS. This targeted-proteomics modality is also known as parallel reaction monitoring (Gallien and Domon, 2015). To improve sensitivity and coverage, we used the enhanced filter-aided sample preparation technique (eFASP) to prepare peptides (Erde et al., 2014). We used as standards two or three heavy-isotope–labeled peptides for each protein, all of which showed linearity when diluted in utricle extracts over the appropriate concentration ranges (Fig. 3, D, G, J, and M). The spiked-in heavy-labeled standards comigrated with unlabeled peptides derived from hair bundles (Fig. 3, E, F, H, I, K, L, N, and O), and all peaks were identified as the correct peptide by searching MS2 spectra against a mouse protein database.

Using targeted MS/MS with heavy standards, we estimated that PLS1, FSCN2, and ESPN were present in hair bundles of P23 CD-1 mice, respectively, at 30,500 ± 700, 16,100 ± 600, and 14,800 ± 500 molecules per stereocilium (Fig. 3 B). Between P4 and P23, the amount of PLS1 and ESPN decreased and that of FSCN2 increased (Fig. 3 B), which was consistent with the shotgun proteomics results (Fig. 3 A). C57BL/6 mice had similar levels of the three cross-linkers, although the ratio of PLS1 to FSCN2 or ESPN was higher in these mice than in CD-1 mice (Fig. 3 C), a trend that was also seen in shotgun experiments.

The amount of ESPN determined by targeted MS/MS analysis was 10-fold higher than estimates from prior mouse (Krey et al., 2015) and chick (Shin et al., 2010, 2013) hair-bundle experiments. Because we suspected that the in-gel protein digest used in previous experiments led to losses of small molecules like the short ESPN splice forms (∼30 kD), we digested embryonic day 20 chicken bundle proteins with trypsin either in SDS gels or directly in the agarose used to capture bundles. Although the estimated concentrations of most proteins were similar in the two experiments, small proteins (<30 kD), including ESPN, were substantially underrepresented in the in-gel digests (Fig. S5). We conclude that although PLS1 and FSCN2 account for ∼85% of the actin cross-linkers in stereocilia, ESPN is present at a substantially higher level than previously appreciated.

Localization of cross-linkers during development

The changes in cross-linker abundance during development were largely corroborated by immunocytochemistry (Fig. 4), where we used directly labeled primary antibodies to improve antibody penetration into the stereocilia actin core (Perrin et al., 2010). PLS1 was readily detected in stereocilia at P1 (Fig. 4 A) and increased in intensity over development. FSCN2 levels were modest at P1 but increased at P8 and P21 (Fig. 4 B). Finally, ESPN levels in stereocilia remained high between P1 and P21; immunoreactivity was highest in the smallest hair bundles (Fig. 4 C). Interestingly, although each of the cross-linkers appeared uniformly distributed in stereocilia, no immunoreactivity was seen for any of them in the taper region at the base of the stereocilia or the rootlets that project into the cell (Fig. 4, A–C).

We also used targeted MS/MS to measure cross-linker abundance during development (Fig. 4, D–F); because we measured levels in whole utricle, the final value was the combination of the hair-bundle and soma concentrations. In whole utricle, PLS1 was much more abundant than either of the other cross-linkers at P1 (Fig. 4, D–F). From P1 to P23, each of the three increased relative to actin (Fig. 4, D–F). During this time period, the number of hair cells more than doubled (Fig. 4, D–F). Although the amount of actin in bundles increases over this same time period, Tilney suggested that hair cells build

Published November 3, 2016

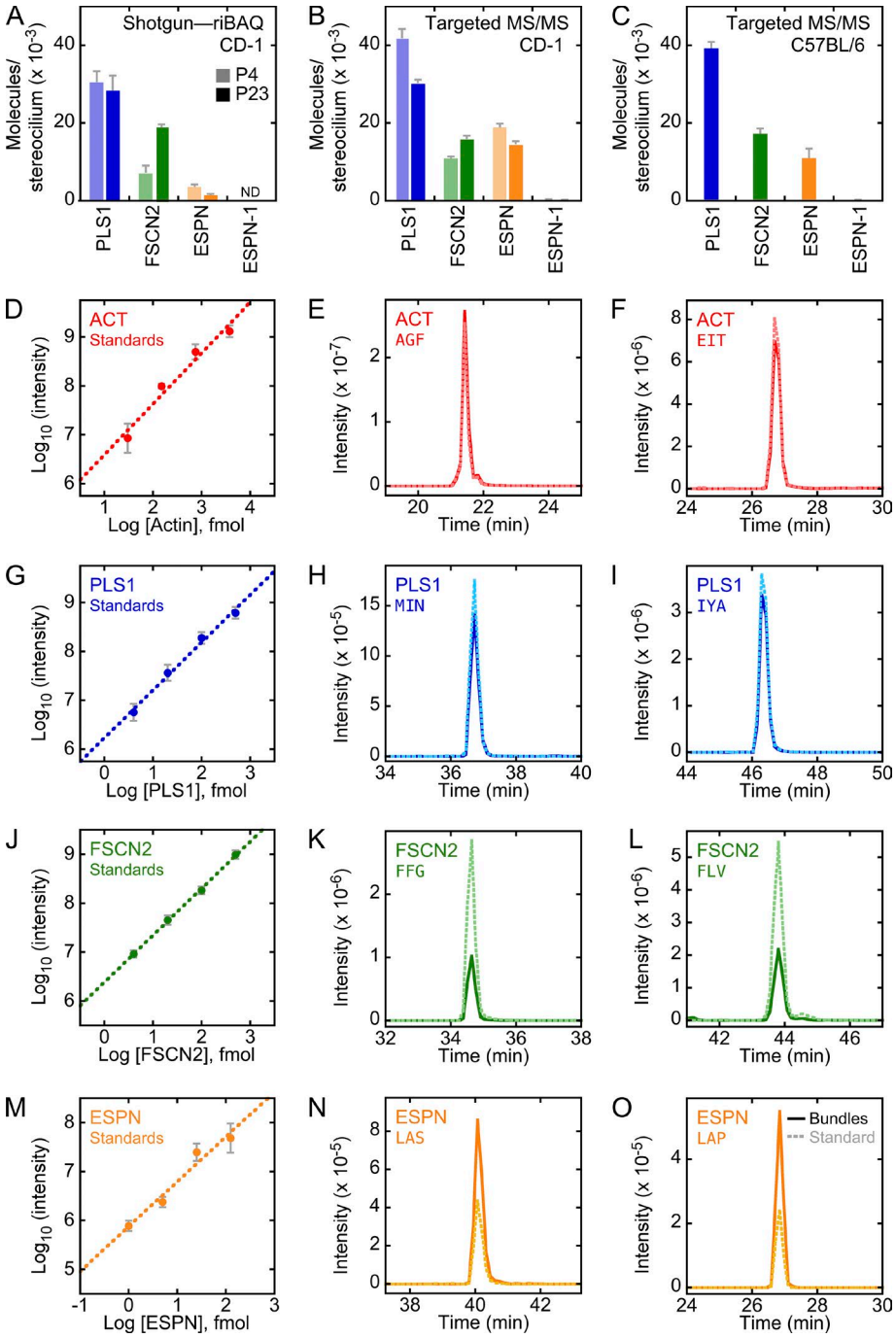

Figure 3. **Targeted proteomics analysis of actin cross-linkers in mouse stereocilia.** (A) Cross-linker quantitation using shotgun MS, derived from MS1 data (Orbitrap riBAQ). Cross-linker quantitation assumes 400,000 actin molecules per stereocilium. (B) Cross-linker quantitation in CD-1 mice using targeted MS/MS using spiked-in heavy-labeled peptide. (C) Cross-linker quantitation in C57BL/6 mice using targeted MS/MS using spiked-in heavy-labeled peptide intensities. Data in A–C are displayed as mean ± SEM. Experimental samples: A, 4 each P5 and P23; B, 4 P5 and 3 P23; C, 4. (D) Actin heavy-isotope peptides analyzed in triplicate by targeted MS/MS (AGFAGDDAPR and EITALAPSTMK combined). Mean ± SEM is displayed (applies to G, J, and M too). (E) Analysis of actin AGFAGDDAPR peptide by targeted MS/MS. Samples in B and C, E and F, H and I, K and L, and N and O contained 10–15 ears' worth of hair bundles, processed using the eFASP method, and 500 fmol (actin), 50 fmol (PLS1 and FSCN2), or 10 fmol (ESPN) of heavy-labeled peptide. (F) Analysis of actin EITALAPSTMK peptide (with oxidized methionine) by targeted MS/MS. (G) PLS1 heavy-isotope peptides analyzed by LC-MS/MS (MINLSEPDTIDER and IYALPD DLVEVKPK combined). (H) Analysis of PLS1 MINLSEPDTIDER (with oxidized methionine) peptide by targeted MS/MS. (I) Analysis of PLS1 IYALPDDLVEVKPK peptide by targeted MS/MS. (J) FSCN2 heavy-isotope peptides analyzed by LC-MS/MS (FFGGIEDR, FLV LPQPDGR, and YLAPVGPAGTLK combined). (K) Analysis of FSCN2 FFGGIEDR peptide by targeted MS/MS. (L) Analysis of FSCN2 FLVLPQPDGR peptide by targeted MS/MS. (M) ESPN heavy-isotope peptides analyzed by LC-MS/MS (LAPWQR and LASLPAWR combined). (N) Analysis of ESPN LASLPAWR peptide by targeted MS/MS. (O) Analysis of ESPN LAPWQR peptide by targeted MS/MS.) For all chromatograms, bundle samples use darker solid lines; heavy-labeled standards use lighter dashed lines.

bundles with a fixed amount of actin (Tilney and Tilney, 1988). The increases seen in whole utricle over development must therefore reflect increased translation of the cross-linkers in each hair cell, not hair cell production. Interestingly, at 4 mo of age, whole-utricle FSCN2 levels remained high, but PLS1 and ESPN levels declined appreciably.

No proteins are up-regulated in hair bundles after loss of PLS1

We used shotgun MS with an ion-trap mass spectrometer to determine whether vestibular hair cells up-regulate or redistribute actin cross-linkers to compensate for the loss of PLS1 (Fig. 5 A). Except for PLS1, there were no significant changes in protein abundance in *Pls1*$^{-/-}$ hair bundles for any of the ∼40 most abundant proteins in hair bundles, including all actin cross-linkers (Fig. 5 A). Moreover, no other protein that might play a cross-linking role (e.g., GAPDH; Waingeh et al., 2006) was present at levels close to that of PLS1 in wild-type or knockout bundles. The lack of up-regulation or redistribution of key stereocilia molecules in *Pls1*$^{-/-}$ mice was confirmed by targeted MS/MS (Fig. 5 B) and protein immunoblotting (Fig. 5, C and D); note that variability in both assays could have obscured a small increase in FSCN2 or ESPN. Thus the absence of PLS1 leads to a partial loss of vestibular function without any significant compensatory expression of other cross-linkers.

Published November 3, 2016

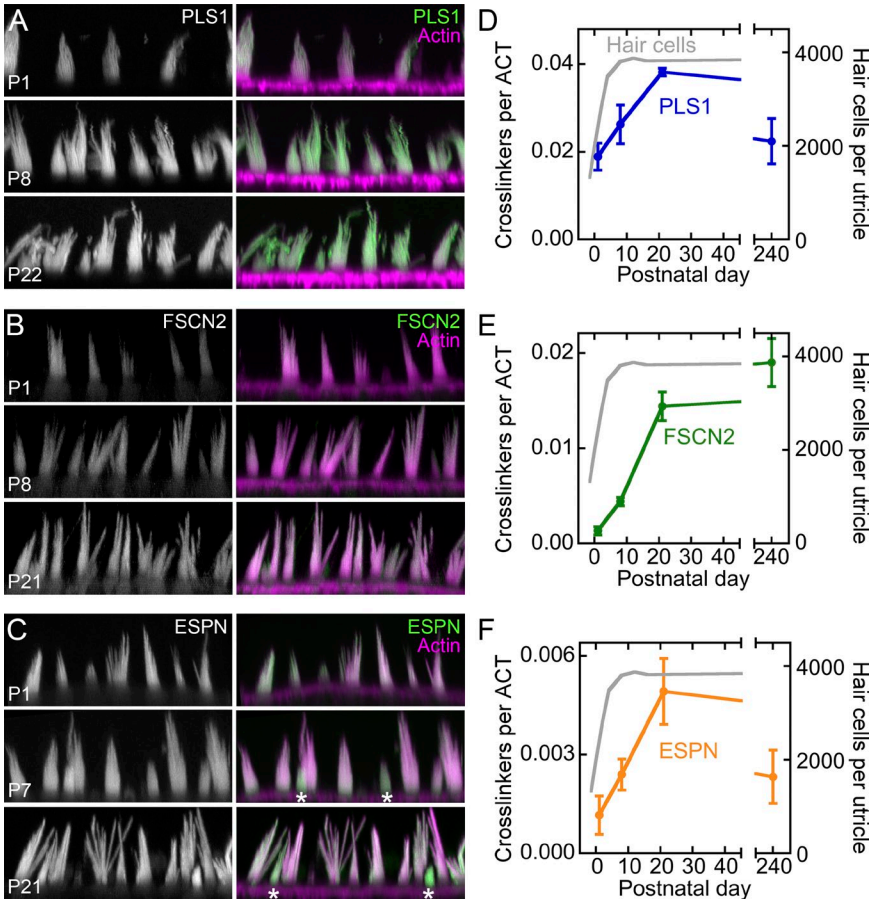

Figure 4. **Expression of stereocilia actin cross-linkers during development.** (A–C) Immunocytochemical localization during utricle development using directly labeled primary antibodies. Stacks of confocal xy images were acquired from whole-mount tissue; xz slices were generated after 3D projection. Each cross-linker was primarily detected in hair bundles. (A) Labeling by Alexa Fluor 488–conjugated anti-PLS1 in bundles increases modestly between P1 and P22. (B) Labeling by Alexa Fluor 568–conjugated anti-FSCN2 in bundles increases substantially between P1 and P22. (C) Labeling by Alexa Fluor 488–conjugated anti-ESPN remains constant after P1. Note that small hair bundles, presumably newly formed, have higher levels of ESPN immunoreactivity (asterisks). All panels are 20 × 50 µm. (D–F) Targeted MS/MS measurement of ratio of cross-linkers to actin during development. Measurements are of whole utricle, not hair bundles. (D) PLS1 is high at P1 and increases moderately after that. (E) FSCN2 is very low at P1 and increases substantially after that; FSCN2 remains high even after 4 mo. (F) ESPN levels are modest at P1 and then increase until P21. Mean ± SEM for three experimental samples for each developmental age.

Stereocilia dimensions are altered in mice lacking functional PLS1

There were, however, significant structural consequences of the *Pls1* knockout in utricular stereocilia. The tallest stereocilia of *Pls1*$^{-/-}$ utricle hair bundles were ∼20% shorter than wild-type stereocilia (Fig. 6, A–C) and stopped lengthening after P7, unlike wild-type stereocilia (Fig. 6 B). Lengths of P21 *Pls1*$^{+/+}$ and C57BL/6 mice were not significantly different (P = 0.2). The shortest stereocilia of *Pls1*$^{-/-}$ bundles were also ∼20% shorter than those of wild type, and the lengths of heterozygous stereocilia were intermediate (Fig. S1 D). Other parameter values describing bundle structure, including bundle array length, bundle slope, and kinocilium length (Li et al., 2008), were not significantly different between wild-type and *Pls1*$^{-/-}$ mice, except for the ratio between kinocilium and stereocilium length (Fig. S1, E–G).

When examined by confocal microscopy, *Pls1*$^{-/-}$ utricular stereocilia appeared to be slightly thinner than those of wild-type utricles (Fig. 6 A). To more accurately determine the diameter of wild-type and mutant stereocilia, we isolated them by adsorption to polylysine-coated glass coverslips (Shepherd et al., 1990) and imaged them using structured illumination microscopy (SIM; Gustafsson, 2000). The relatively narrow point-spread function of this microscopy modality permits a more accurate determination of diameter than conventional confocal microscopy (Gustafsson, 2000). *Pls1*$^{-/-}$ stereocilia were indeed thinner (Fig. 6, D–F); this observation was corroborated by the reduced phalloidin signal (Fig. 6 D), which indicated that mutant stereocilia had less F-actin. As with the lengthening, widening largely ceased in *Pls1*$^{-/-}$ stereocilia after P7 (Fig. 6 E). Stereocilia that are 20% shorter and 20% thinner should have only half as much actin as wild-type stereocilia; indeed, protein immunoblotting indicated that *Pls1*$^{-/-}$ stereocilia had an actin content only ∼60% that of wild-type stereocilia (Fig. 5, C and D).

Stereocilia of *Fscn2*$^{R109H/R109H}$ utricles were normal both in length and diameter (Fig. 6, C and F). Moreover, hair bundles of *Pls1*$^{-/-}$ *Fscn2*$^{R109H/R109H}$ double mutant mice were also relatively normal in appearance (Fig. 6 A), but their stereocilia dimensions were identical to those of *Pls1*$^{-/-}$ mice (Fig. 6, C and F). These results show that PLS1 is essential for the lengthening and widening of stereocilia during late postnatal development.

PLS1 shifts actin-filament packing from hexagonal to liquid

The internal structure of utricle stereocilia changed substantially with the loss of *Pls1;* strikingly, the liquid packing seen in wild type was replaced with robust hexagonal packing in *Pls1*$^{-/-}$ stereocilia (Figs. 7 and 8). Packing of actin filaments in stereocilia can be analyzed by optical diffraction (DeRosier and Moore, 1970; DeRosier and Tilney, 1982), where a frequency-domain image resulting from a fast Fourier transformation (FFT) displays the geometric characteristics (like repeat intervals) of the spatial-domain image. Using transmission EM, we examined thin sections of stereocilia processed using freeze substitution. Optical diffraction analysis of transverse sections showed the change in packing clearly; although the FFT of wild-type stereocilia revealed a circular feature corresponding to liquid packing (Fig. 7, A–D), the FFT of *Pls1*$^{-/-}$ stereocilia actin cores always produced a hexagonal pattern (Fig. 7, E–H).

Published November 3, 2016

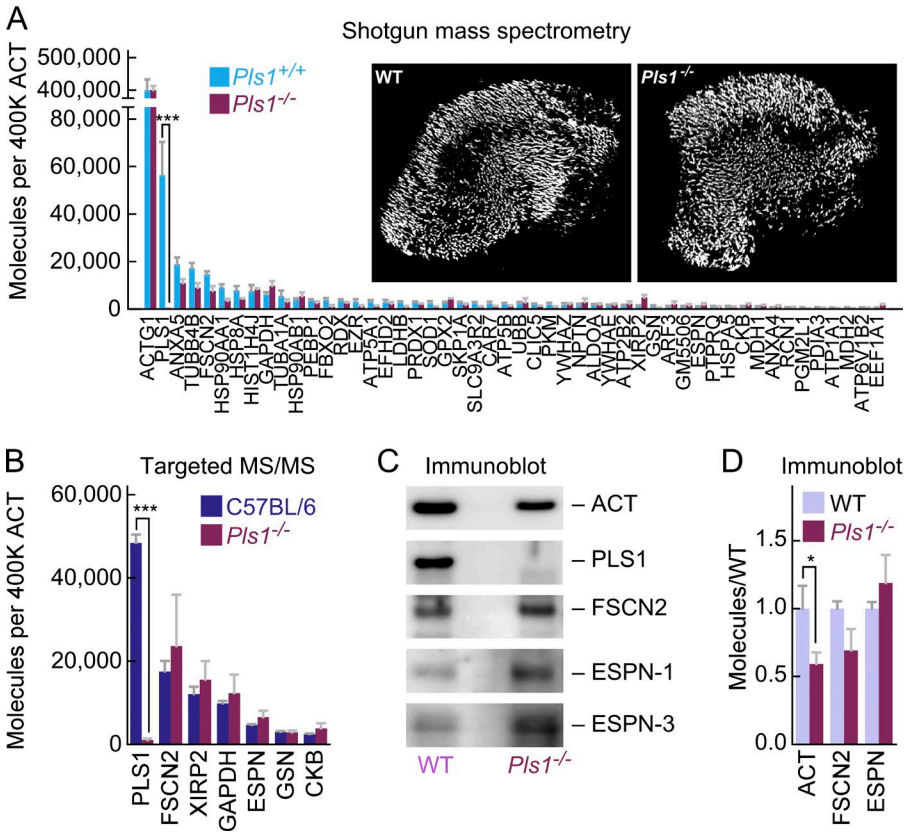

Figure 5. **Lack of compensation by other cross-linkers in *Pls1*$^{-/-}$ mice.** Comparison of wild-type and *Pls1*$^{-/-}$ utricle hair bundles. (A) Quantitation by shotgun MS using MS2 intensities; molecules per 400,000 actin monomers were plotted. Note loss of PLS1 in *Pls1*$^{-/-}$ bundles (***; P = 10^{-7}, adjusted for false-discovery rate). No other protein changed significantly in abundance. Four experimental samples each of *Pls1*$^{+/+}$ and *Pls1*$^{-/-}$ stereocilia were run (each with 15 ear equivalents); mean ± SEM. Inset, isolated hair bundles stained with phalloidin from wild-type and *Pls1*$^{-/-}$ utricles (panel full widths, 481 µm). (B) Targeted MS/MS analysis using endogenous peptide intensity of indicated proteins. Three C57BL/6 and two *Pls1*$^{-/-}$ experimental samples were run, each with 10 ear equivalents; mean ± SEM. The only protein that showed a significant difference (by two-tailed Student's *t* test) was PLS1 (***; P = 0.0003). (C) Protein immunoblots; wild-type (WT) animals were a mix of *Pls1*$^{+/+}$ and C57BL/6. Equal numbers of hair bundles loaded in WT and *Pls1*$^{-/-}$ lanes. Note the reduced signal for actin in *Pls1*$^{-/-}$ bundles, as well as the complete loss of PLS1. (D) Immunoblot quantitation; equal numbers of hair bundles loaded. WT also has a mixture of *Pls1*$^{+/+}$ and C57BL/6. Only actin was significantly changed in *Pls1*$^{-/-}$ as compared with WT (*, P = 0.015). Experimental samples: actin, 8 WT and 10 *Pls1*$^{-/-}$; FSCN2, 4 WT and 5 *Pls1*$^{-/-}$; ESPN, 3 WT and 4 *Pls1*$^{-/-}$. Mean ± SEM are plotted.

Consistent with measurements with structured-illumination microscopy, the actin paracrystal was significantly more narrow in *Pls1*$^{-/-}$ stereocilia (149 ± 31 nm, n = 118) than in wild-type stereocilia (169 ± 36 nm, n = 106; P = 10^{-5} by Student's *t* test). The distance from the center to the dense features in the Fourier transform corresponds to the inverse of the actin-filament spacing, which showed that actin filaments were more tightly packed in *Pls1*$^{-/-}$ than in wild-type stereocilia (Fig. 7 K).

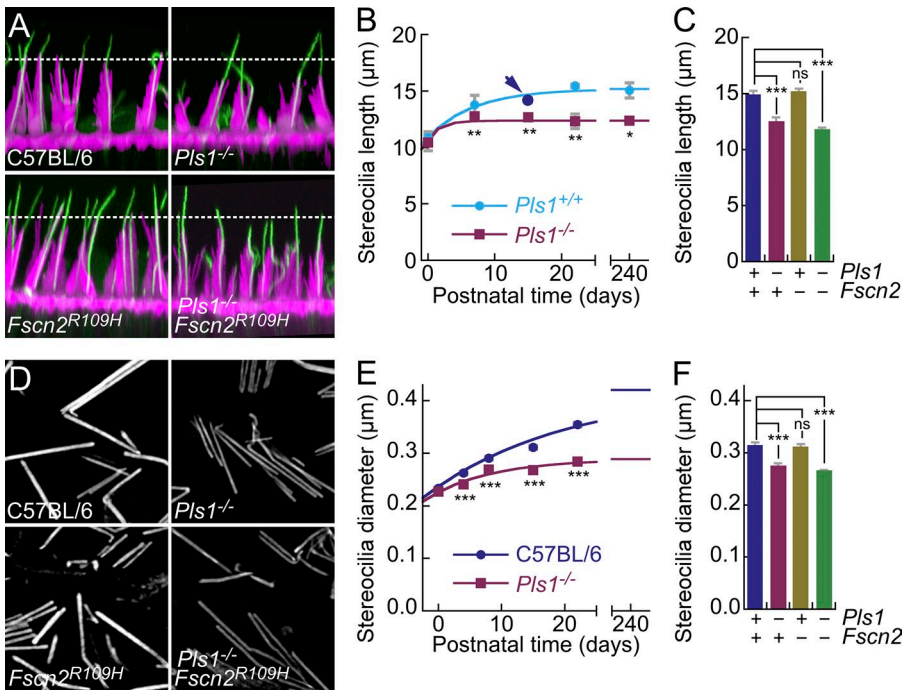

Figure 6. ***Pls1*$^{-/-}$ stereocilia are shorter and narrower than those of wild-type mice.** (A) Confocal immunocytochemistry of whole-mount utricles from indicated genotypes. Magenta, actin; green, acetylated tubulin. Panels are 35 µm wide. (B) Quantitation of tallest stereocilia length from confocal stacks. All wild-type points were from *Pls1*$^{+/+}$ mice, except that P15 was C57BL/6 (arrow). Mean ± SEM are plotted. Significance levels of differences between wild-type and *Pls1*$^{-/-}$ are indicated. Measurements: P4, 64 *Pls1*$^{+/+}$ and 58 *Pls1*$^{-/-}$; P7, 47 *Pls1*$^{+/+}$ and 49 *Pls1*$^{-/-}$; P15, 44 *Pls1*$^{+/+}$ and 49 *Pls1*$^{-/-}$; P21, 28 *Pls1*$^{+/+}$ and 34 *Pls1*$^{-/-}$; 4 mo, 59 *Pls1*$^{+/+}$ and 57 *Pls1*$^{-/-}$. (C) Tallest stereocilia length at P23 for the indicated genotypes. Mean ± SEM are plotted. Measurements: 114 C57BL/6, 59 *Pls1*$^{-/-}$, 106 *Fscn2*$^{R109H/R109H}$, and 85 *Pls1*$^{-/-}$ *Fscn2*$^{R109H/R109H}$. (D) SIM imaging of stereocilia isolated by adherence to glass coated with poly-L-lysine. Panels are 13 µm wide. (E) Quantitation of stereocilia width from structured illumination microscopy images. Mean ± SEM are plotted. Six experiments at each age and genotype were averaged for the figure. (F) Stereocilia width at P21 for the indicated genotypes. Mean ± SEM are plotted. Measurements: 75 C57BL/6, 126 *Pls1*$^{-/-}$, 146 *Fscn2*$^{R109H/R109H}$, and 147 *Pls1*$^{-/-}$ *Fscn2*$^{R109H/R109H}$. In B, C, E, and F, data are mean ± SEM. *, P < 0.05; **, P < 0.01; ***, P < 0.001; ns, not significant.

Published November 3, 2016

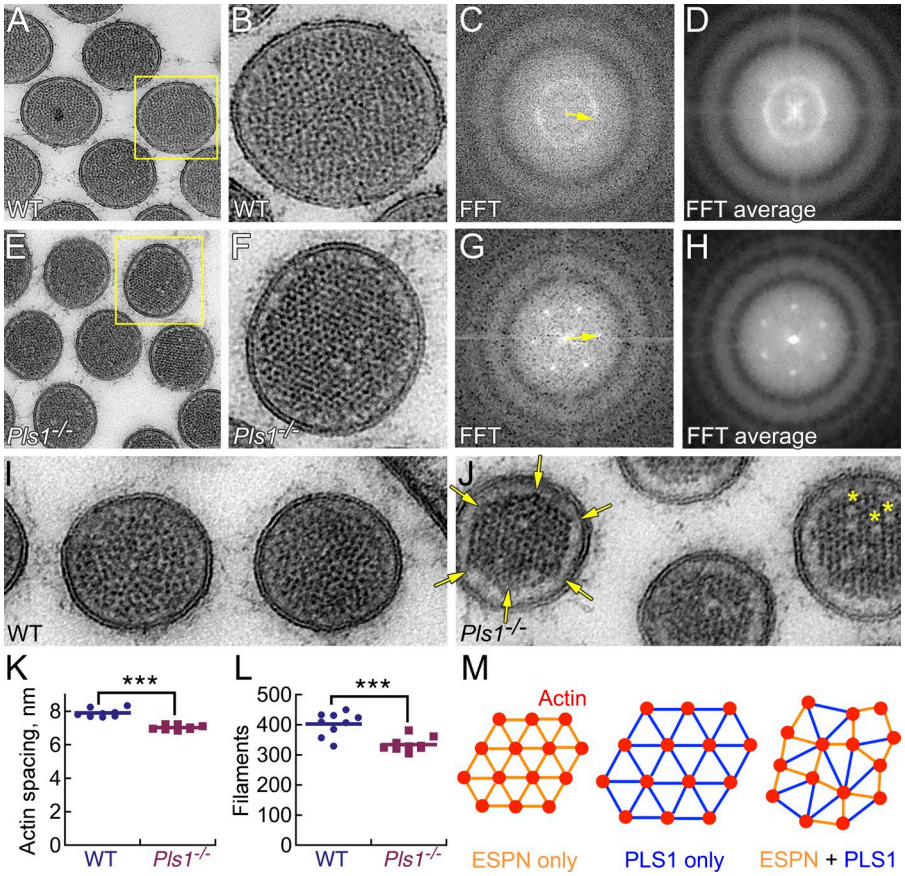

Figure 7. **Utricle *Pls1*$^{-/-}$ stereocilia actin filaments have hexagonal packing.** Stereocilia were prepared for transmission EM using freeze substitution. (A) Transverse section through wild-type (C57BL/6) stereocilia; box indicates area enlarged in B. (B) Single wild-type stereocilium (spatial domain). (C) Cropped FFT of stereocilium in B (frequency domain). Arrow indicates distance of 8.4 nm in inverse space. (D) Mean of FFTs from 11 wild-type stereocilia from the uncropped image in A. (E) Transverse section through *Pls1*$^{-/-}$ stereocilia; box indicates area used for F. (F) Single *Pls1*$^{-/-}$ stereocilium. (G) Cropped FFT of stereocilium in E. Arrow indicates distance of 7.3 nm in inverse space. (H) Mean of FFTs from 10 *Pls1*$^{-/-}$ stereocilia from the uncropped image of E. (I) Narrow wild-type stereocilia; normal liquid packing. (J) Narrow *Pls1*$^{-/-}$ stereocilia. Arrows highlight vertices of hexagonal actin paracrystal; asterisks indicate gaps where actin filaments are missing from the paracrystal. (K) Actin center-to-center spacing from FFT analysis. Bar indicates the mean. ***, P = 10^{-7} by two-tailed Student's *t* test. (L) Filament count. Bar indicates the mean. ***, P = 10^{-4}. (M) Model for actin filament packing with cross-linkers of different lengths. (left) ESPN alone allows hexagonal packing. (middle) PLS1 (modeled as ~25% longer cross-link distance than ESPN) alone also allows hexagonal packing. (right) Mixture of ESPN and PLS1 prevents hexagonal packing. Panel full widths: (A and E) 600 nm; (B and F) 230 nm; (I and J) 468 nm (same scale as B and F).

In addition, the number of actin filaments in *Pls1*$^{-/-}$ stereocilia (335 ± 23, $n = 9$) was significantly reduced relative to the number in wild-type stereocilia (403 ± 39, $n = 9$; P = 10^{-4}; Fig. 7 L). The decreased diameter of the actin core of *Pls1*$^{-/-}$ stereocilia thus arises from both fewer actin filaments and tighter packing.

Using FFT analysis of small regions or Fourier mask analysis, we saw no evidence for local hexagonal packing within wild-type stereocilia; packing appeared to be uniformly liquid. Likewise, immunogold EM with anti-ESPN antibodies indicated that the distribution of ESPN was not significantly different in cross sections of wild-type and *Pls1*$^{-/-}$ stereocilia (Fig. S1, H–J).

Images of narrow *Pls1*$^{-/-}$ stereocilia, likely taken near the stereocilia base, showed that not only was the packing of the actin filaments hexagonal, but also the actin paracrystal itself could be hexagonal (Fig. 7 J, arrows). In addition, some *Pls1*$^{-/-}$ stereocilia had gaps where filaments were missing (Fig. 7 J, asterisks); gaps were rarely observed in wild-type stereocilia. Tapers, rootlets, and tips of *Pls1*$^{-/-}$ stereocilia appeared normal.

Actin packing in single and double mutants

We also compared all four genotypes using transmission EM with dehydration processing (Fig. 8). Although membranes were more poorly preserved with this method, the liquid-to-hexagonal shift in actin-filament packing was also seen when wild-type and *Pls1*$^{-/-}$ stereocilia were compared (Fig. 8, A and B). Analysis of the Fourier features showed that although filaments were spaced 9.7 ± 0.8 nm (mean ± SD, $n = 96$) in wild-type stereocilia, they were spaced only 7.9 ± 0.6 nm ($n = 97$) in *Pls1*$^{-/-}$ stereocilia.

The packing arrangement of actin filaments in stereocilia of *Fscn2*$^{R109H/R109H}$ utricles was similar to that in wild-type stereocilia; Fourier analysis indicated that the packing was liquid (Fig. 8 C). At 10.4 ± 0.7 nm ($n = 104$), the spacing between actin filaments in *Fscn2*$^{R109H/R109H}$ stereocilia was significantly greater than that in wild-type stereocilia. In contrast, packing of filaments in *Pls1*$^{-/-}$ *Fscn2*$^{R109H/R109H}$ double-mutant mice was hexagonal, with no apparent differences from that of *Pls1*$^{-/-}$ stereocilia (Fig. 8 D); actin-filament spacing in these stereocilia was 8.9 ± 0.5 nm ($n = 102$).

We used a multivariate ANOVA analysis to determine the statistical significance of the addition of each cross-linker as compared with the ESPN-only state (*Pls1*$^{-/-}$ *Fscn2*$^{R109H/R109H}$). Addition of either PLS1 (*Fscn2*$^{R109H/R109H}$ mice) or FSCN2 (*Pls1*$^{-/-}$ mice) significantly changed the actin-filament spacing (P < 10^{-3}), albeit with different polarities. Actin filaments in stereocilia with all three cross-linkers (wild type) were also spaced more widely apart from those with ESPN alone (P = 0.014), indicating that the effect of PLS1 on spacing outweighed that of FSCN2.

Loss of PLS1 causes changes in actin packing in cochlear stereocilia

Given the auditory phenotype seen in *Pls1*$^{-/-}$ mice (Fig. 2, A and B), we examined whether stereocilia structure was affected in outer or IHCs of P23 cochleas (Fig. 9, A and B, top row). In OHCs, like in utricle hair cells, *Pls1*$^{-/-}$ stereocilia actin cores were smaller in diameter when compared with wild type (169 ± 22 vs. 186 ± 21 nm; P = 10^{-11}). Moreover, FFT transformation showed that wild-type OHC stereocilia had liquid packing of their actin filaments, whereas *Pls1*$^{-/-}$ stereocilia had hexagonal packing (Fig. 9, A and B, bottom row).

Published November 3, 2016

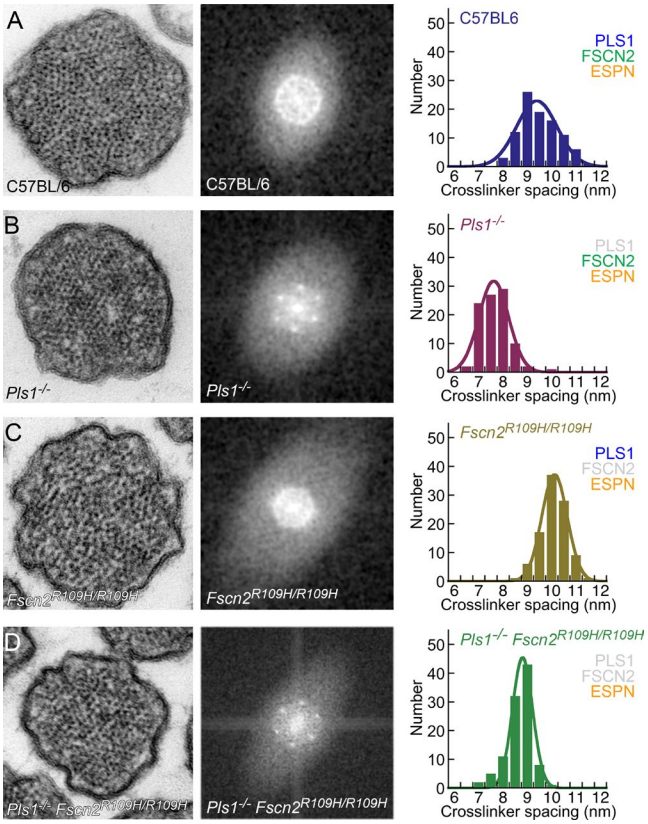

Figure 8. **Packing of actin filaments in single and double mutants.** Stereocilia were prepared for transmission EM using dehydration. (left) Stereocilia cross sections from indicated genotypes; all panels are 300 nm wide. (middle) Cropped FFT transforms of spatial images. (right) Distribution of cross-linker distance determined by FFT analysis and fit with a single Gaussian function. (A) Wild type (C57BL/6). The ring in the FFT image indicates liquid packing. (B) *Pls1*$^{-/-}$. These stereocilia had six peaks of equal intensity in FFT, which indicates hexagonal packing. (C) *Fscn2*$^{R109H/R109H}$. The FFTs from these stereocilia displayed a ring with some hexagonal definition. (D) *Pls1*$^{-/-}$ *Fscn2*$^{R109H/R109H}$ double mutants. These stereocilia had six peaks in the FFT like in *Pls1*$^{-/-}$, but often two opposing peaks were more intense than the four flanking peaks.

Stereocilia of *Pls1*$^{-/-}$ IHCs have reduced diameters as compared with wild-type stereocilia (Taylor et al., 2015). Like in other stereocilia, FFTs indicated a high degree of hexagonal actin-filament packing in stereocilia of *Pls1*$^{-/-}$ IHCs (Fig. 9 D). Surprisingly, many wild-type IHC stereocilia images had a composite liquid-hexagonal structure revealed by FFT (Fig. 9 C). When we used a Fourier mask to reveal the location of highly hexagonal regions of these wild-type stereocilia, we found that central regions had a higher degree of hexagonal packing (Fig. 9 E). In *Pls1*$^{-/-}$ IHCs, nearly the entire paracrystal was hexagonally packed (Fig. 9 F), as with OHC and vestibular stereocilia.

Discussion

Hair cells rely on three different cross-linkers to produce the composite properties of the actin paracrystal cores of their stereocilia. Despite its comparatively low abundance, ESPN is the most critical cross-linker of stereocilia; this conclusion is reinforced by the severity of the stereocilia structural phenotype in *deaf jerker* mice (Zheng et al., 2000; Sekerková et al., 2011) and the complete loss of VsEPs in these mice (Jones et al., 2005). We found that loss of PLS1 and FSCN2 also affects vestibular function and stereocilia structure, but with notably milder phenotypes. Stereocilia grew to their wild-type length and width only if PLS1 was present, suggesting that the liquid packing of actin filaments mediated by PLS1 may be necessary for stereocilia to grow to their proper dimensions. By contrast, loss of FSCN2 did not impact stereocilia dimensions, consistent with its ability to stabilize the actin core during rapid hair-bundle stimulation but allow actin dynamics at longer timescales (Hwang et al., 2015). Formation of normal mouse vestibular stereocilia thus requires both ESPN and PLS1, but long-term stereocilia maintenance (at least in mouse cochlea) depends on FSCN2 (Perrin et al., 2013). Consistent with those conclusions, FSCN2 expression remained high in the oldest utricles we examined, whereas PLS1 and ESPN levels were reduced.

In mouse utricle, there were ∼68,000 total cross-linkers per 400,000 actin monomers, close to the theoretical maximum of ∼90,000 (Shin et al., 2013). PLS1 was the most abundant of the cross-linkers (∼60% of the total), as well as the second most abundant protein overall; FSCN2 (∼25%) and ESPN (∼15%) were less abundant. The ESPN concentration we report here is considerably higher than that previously estimated using shotgun proteomics with in-gel trypsin digestion (Shin et al., 2010, 2013; Krey et al., 2015), reinforcing the value of the more rigorous targeted MS/MS approach with eFASP peptide preparation. Similar inaccuracies may apply to other proteins quantified with in-gel digestion and shotgun MS, particularly those of low molecular mass.

Although not statistically significant, both shotgun proteomics (Fig. 5 A) and immunoblotting (Fig. 5 D) indicated that the ESPN/actin ratio was increased approximately twofold in *Pls1*$^{-/-}$ stereocilia as compared with wild-type stereocilia. If the ESPN abundance measured by targeted MS/MS analysis is used, these results suggest that somewhat more ESPN might be present in mutant stereocilia than in those of wild-type animals. There was no evidence for up-regulation of FSCN2, however.

Mice lacking functional PLS1 or FSCN2 have auditory and vestibular dysfunction

Pls1$^{-/-}$ and *Fscn2*$^{R109H/R109H}$ mice each display progressive hearing loss that correlates with morphological defects in cochlear stereocilia (Perrin et al., 2013; Taylor et al., 2015). We confirmed those observations and showed additionally that *Pls1*$^{-/-}$ *Fscn2*$^{R109H/R109H}$ mice have an auditory phenotype that is even more severe. Interestingly, *Pls1*$^{-/-}$ mice were strongly affected at low frequencies (<15 kHz) in measurements of ABRs, but not of distortion product otoacoustic emissions. By contrast, at low frequencies, ABR thresholds for *Fscn2*$^{R109H/R109H}$ mice were normal, but DPOAE amplitudes were reduced. These results suggest that at low frequencies, the *Pls1* mutation more strongly affected IHCs, whereas the *Fscn2* mutation more strongly affected OHCs.

Because we can use proteomics to characterize utricle hair bundles, our focus here is on vestibular hair cells and their function. Thresholds for detecting vestibular-evoked potentials in mice with mutations in *Pls1* or *Fscn2* were substantially elevated, suggesting reduced vestibular function. Double mutants were even more affected. p1 latencies, n1 latencies, and p1-n1 amplitudes were all affected by the cross-linker mutations. When stimulus values were normalized for threshold, however, the functions overlap; this result suggests that differences

Published November 3, 2016

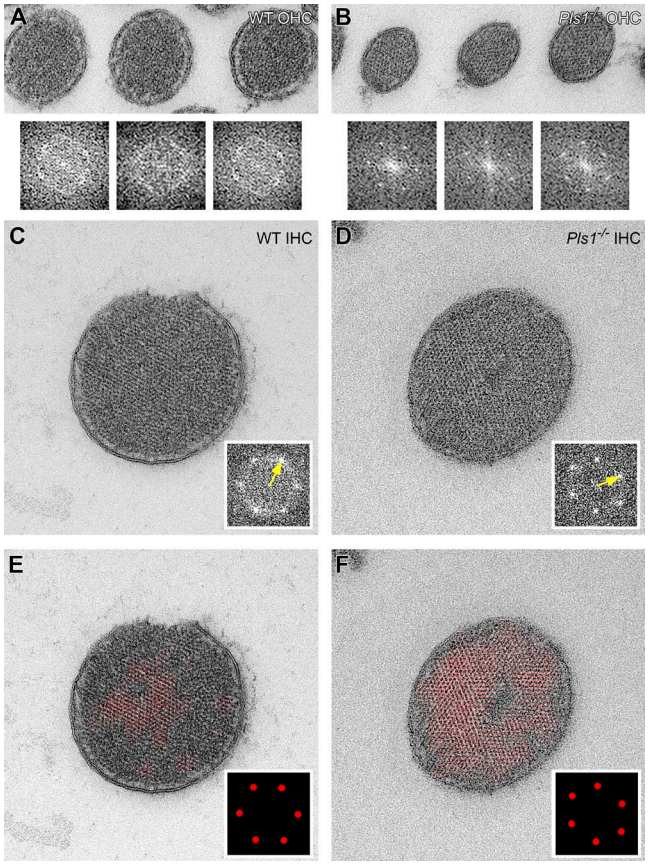

Figure 9. **Packing of actin filaments in cochlear stereocilia.** Stereocilia were prepared for transmission EM using freeze substitution. Transverse sections of cochleas prepared with freeze substitution. (A and B) OHC stereocilia from wild-type and *Pls1*$^{-/-}$ stereocilia. Panels are 700 nm wide. The bottom rows show FFT transforms of the three stereocilia in each image. In the A FFTs, the circular features (in inverse space) indicate mean filament spacing of 7.9, 7.6, and 7.4 nm. In the B FFT, the hexagonally arranged points (in inverse space) indicate mean filament spacing of 7.9, 7.9, and 7.8 nm. (C and D) IHC stereocilia from wild-type and *Pls1*$^{-/-}$ stereocilia. Panels are 700 nm wide. Insets, cropped FFT images. Yellow arrows: A, 8.2 nm in inverse space (mean of all six spots); B, 8.7 nm in inverse space. (E and F) IHC stereocilia from wild-type and *Pls1*$^{-/-}$ stereocilia. Insets, cropped masks used for Fourier filtering (in inverse space).

seen in latency and amplitude were primarily caused by threshold differences in the genotypes. Thus, the loss of vestibular function in mutant animals was primarily caused by reduced end-organ sensitivity rather than changes in neural timing or synchrony; this conclusion is consistent with PLS1 and FSCN2 expression, which is restricted to hair cells. We also noted that *Pls1*$^{-/-}$, *Fscn2*$^{R109H/R109H}$, and *Pls1*$^{-/-}$ *Fscn2*$^{R109H/R109H}$ mice did not exhibit overt behavior that correlated with loss of vestibular function (e.g., circling); as long as ESPN was present, stereocilia formed relatively normally and vestibular function was only partially reduced.

These results suggest that formation of functional stereocilia actin paracrystals may not require extensive cross-linking, at least in the vestibular system. Although reducing the concentration of cross-linkers will decrease the stiffness of an individual stereocilium, this reduction should have almost no effect on overall hair-bundle stiffness; the taper region and the interstereocilia links dominate bundle compliance (Hudspeth, 1989) and are much more compliant than a paracrystal with hundreds of actin filaments, whether they are heavily cross-linked or not (Gardel et al., 2004).

Assembly of actin paracrystals by rigid and flexible cross-linkers

Actin filaments lack perfect helical symmetry, and opposing subunits on adjacent filaments are not optimally positioned to be bridged by a cross-linker (DeRosier and Tilney, 1984; Claessens et al., 2008). To form a cross-linked actin paracrystal, either filaments must be twisted by rigid cross-linkers or cross-linkers must exhibit enough flexibility to accommodate the mismatches (Claessens et al., 2008). Indeed, the actin polymer exhibits a significant amount of angular disorder between adjacent subunits (Egelman et al., 1982; DeRosier and Tilney, 1984), which suggests that filaments have enough intrinsic flexibility to twist; still, the twist must be driven by cross-linkers. Each of the three cross-linker families is thought to bind actin differently and produce different amounts of twist in the actin helical structure (Claessens et al., 2008).

Espin forms rigid cross-links and induces overtwisting of actin filaments at low stoichiometry (Purdy et al., 2007; Claessens et al., 2008; Shin et al., 2009), properties that are ideal for controlling the diameter of an actin paracrystal. By contrast, fascins form flexible, rapidly reversible cross-links that can be incorporated during or after actin polymerization (Vignjevic et al., 2006; Claessens et al., 2008; Shin et al., 2009); these properties are ideal for a cross-linker that is used to stabilize a preformed actin paracrystal or for a homogeneous actin structure that relies on a single cross-linker. Consistent with this view, Fscn2b of zebrafish stereocilia is highly dynamic (Hwang et al., 2015). Finally, plastins are also flexible cross-linkers but must be present during actin-filament polymerization to incorporate into a paracrystal (Volkmann et al., 2001).

ESPN and PLS1 are expressed early during hair-bundle formation, followed later by FSCN2. Although the total amount of ESPN in the mouse utricle increases between P5 and P23, the amount per stereocilium decreases modestly (Fig. 3 B). Immunocytochemistry indicated that ESPN is at its highest level relative to actin in small bundles (Fig. 4 C), which are presumably newly formed. PLS1 also acts early; although the PLS1/actin ratio doubled in whole utricle between P1 and P23, the ratio remained constant in bundles between P5 and P23, indicating that PLS1 levels at P5 were sufficient to saturate stereocilia binding sites. Finally, FSCN2 expression in the whole utricle increased 10-fold between P1 and P23, and the ratio of FSCN2 to actin in stereocilia increased over this period as well (Fig. 3). The physical properties of fascins coupled with this expression pattern suggest that FSCN2 enters stereocilia late, stabilizing paracrystals already formed by ESPN and PLS1.

These interpretations are supported by results with mutant mice. The *deaf jerker* mouse phenotype, which includes primary effects on stereocilia diameter and secondary effects on length in both auditory and vestibular hair cells, supports an essential role for ESPN (Zheng et al., 2000; Sekerková et al., 2011). Reduced length and width of stereocilia lacking PLS1, corresponding to a ∼40% reduction of filamentous actin (corroborated by the immunoblotting results of Fig. 5 [C and D] and the filament numbers of Fig. 7 L), suggests that PLS1 drives stereocilia expansion, especially during later stages. In contrast, *Fscn2*^{R109H} stereocilia do not show length or diameter defects, consistent with a role for FSCN2 in structural support, but not actin paracrystal dimensions.

Stereocilia form their actin cytoskeleton nearly normally with only ESPN as their actin cross-linker. ESPN has several roles in stereocilia, however, as the ESPN-1 splice form is thought to

Published November 3, 2016

control stereocilia elongation by its local action at stereocilia tips (Salles et al., 2009; Merritt et al., 2012; Ebrahim et al., 2016). *Espn-1* knockout mice have mostly normal stereocilia (Ebrahim et al., 2016), implying that the shorter ESPN isoforms are crucial for assembling stereocilia. Still, hair bundles initially form with nearly normal morphology in the *deaf jerker* mouse, which suggests that the combination of PLS1 and FSCN2 is sufficient to form a bundle with distinct stereocilia of systematically varying heights. The final form of the bundle thus requires multiple cross-linkers, yet bundles formed with only one or two cross-linkers still function sufficiently well to allow the inner ear to function.

Control of actin-paracrystal properties using multiple cross-linkers

What features are gained by the use of a composite actin-cross-linker matrix? Use of more than one cross-linker allows for different packing of actin filaments. Two uniform packing arrangements are possible with actin filaments: hexagonal and tetragonal. Both arrangements use the same bonding rules, but successive cross-linkers bind at 60° and 90° intervals, respectively (DeRosier et al., 1980). Although there is no evidence in vivo for tetragonal packing, many stereocilia, including those from lizard (Tilney et al., 1980) and mouse (Mogensen et al., 2007), show liquid packing, which is intermediate between hexagonal and tetragonal (DeRosier et al., 1980; DeRosier and Tilney, 1984). Our data show that in the absence of PLS1, mouse stereocilia revert to hexagonal packing of their actin filaments, demonstrating that PLS1 drives liquid packing in stereocilia. Although either ESPN alone or PLS1 alone can produce hexagonal filament packing, mismatched cross-linker lengths when both cross-linkers are used leads to liquid packing (Fig. 7 M). Other data indicate that PLS1 induces liquid packing in stereocilia. Hair bundles of both chicken utricles and chicken cochlea have much more FSCN2 than PLS1 (Shin et al., 2013; Avenarius et al., 2014), and actin filaments are packed hexagonally in each (Tilney and DeRosier, 1986; Shin et al., 2013).

Liquid packing confers several advantages to wild-type stereocilia. First, the maximal number of cross-linkers required will be reduced by ∼20% (DeRosier and Tilney, 1984). Second, the entropy of a disordered paracrystal will be favorable, and liquid packing may correspond to a local energy minimum (DeRosier and Tilney, 1984). Finally, liquid packing should allow the diameter of the paracrystal to grow much larger. Actin paracrystals formed with single cross-linkers reach a maximum diameter in vitro of 50–200 nm (Claessens et al., 2008; Jansen et al., 2011); the maximum is likely reached when internal strain increases as the actin paracrystal grows larger. The use of more than one cross-linker therefore allows the actin core of a stereocilium to increase beyond this limit.

Materials and methods

Antibodies

The mouse monoclonal anti–PLS1 antibody was purchased from Abnova (clone 3G10, H00005357-M04), and the rabbit polyclonal anti–ESPN antibody (against all isoforms) was generated in the Kachar laboratory (PB127). For direct immunostaining, each antibody was conjugated to Alexa Fluor 488 dye using an Alexa Fluor 488 Antibody Labeling kit according to the kit's instructions (Invitrogen). Alexa Fluor 568–conjugated anti–FSCN2 antibody was provided by B. Perrin (Indiana University–Purdue University Indianapolis, Indianapolis, IN; Perrin et al., 2013). A mouse monoclonal anti–actin antibody (JLA-20; Developmental Studies Hybridoma Bank), rabbit polyclonal anti–FSCN2 antibody (#37 against peptide CYTLEFKAGKLAFKD; Shin et al., 2010), rabbit polyclonal anti–ESPN (C terminus) antibody (provided by S. Heller, Stanford University, Palo Alto, CA), and Abnova anti-PLS1 were used for immunoblotting.

Mutant mice

Production of *Pls1*$^{-/-}$ has been described previously (Grimm-Günter et al., 2009; Revenu et al., 2012; Taylor et al., 2015); we maintained them on a C57BL/6J background by periodic backcrossing to C57BL/6. This line was the same as that used for characterization of the auditory system (Taylor et al., 2015). We also maintained a colony of *Pls1*$^{+/+}$ mice that were derived from the original *Pls1* targeting experiments; these mice have not been backcrossed to C57BL/6 and have apparently suffered some genetic drift. All results in the vestibular system were the same for C57BL/6 and *Pls1*$^{+/+}$ mice; the two strains only differed in the auditory system, where at high frequencies, the sensitivity of *Pls1*$^{+/+}$ mice was reduced relative to C57BL/6. We used separate mutant and wild-type colonies for the proteomics experiments to eliminate the need to discard heterozygous animals, which would be generated by *Pls1*$^{+/-}$ incrossing. Because they harbor the R109H mutation of FSCN2 (Shin et al., 2010), we used DBA2/J (D2) mice for early experiments with mutant FSCN2. Results reported here, however, were all from B6.D2-*Fscn2*^{ahl8}/4Kjn (Perrin et al., 2013), a homozygous subcongenic line that we refer to as *Fscn2*^{R109H}. These mice, which are available from The Jackson Laboratory (stock 009629), have a mostly C57BL/6 background except for a small region surrounding the *Fscn2* gene, which is derived from the D2 genome (Perrin et al., 2013). Results were similar with D2 and *Fscn2*^{R109H} mice. The *Fscn2*^{R109H} line was maintained by incrossing (two to five generations for the animals in this study). We generated *Pls1*$^{-/-}$ *Fscn2*$^{R109H/R109H}$ double mutants by standard breeding techniques; this line was also maintained by incrossing (two to five generations for the animals in this study). If not otherwise noted, wild-type mice were C57BL/6. All experiments were performed in accordance with the US Department of Health and Human Services Guide for the Care and Use of Laboratory Animals; animal research was reviewed and approved by institutional animal care and use committees at Oregon Health and Science University and University of Nebraska-Lincoln.

Inner ear functional measures

Functional studies were completed for the following strains at 2 mo of age: C57BL/6, *Pls1*$^{+/+}$ wild type, *Pls1*$^{+/-}$ heterozygote, *Pls1*$^{-/-}$ homozygote, *Fscn2*^{R109H}, and *Pls1*$^{-/-}$ *Fscn2*^{R109H}. Mice were anesthetized by intraperitoneal injection of ketamine and xylazine (18 and 2 mg/ml; 5–7 µl/g body weight), followed by maintenance doses of 50 µl every 60 min or as needed to maintain adequate anesthesia. Core body temperature was maintained at 37.0 ± 0.2°C using a homeothermic heating pad (FHC, Inc.). Recording electrodes were placed subcutaneously at the nuchal crest (noninverting electrode), behind the right pinna (inverting electrode), and at the hip (ground electrode). Functional measures were completed in the following order: DPOAEs, ABRs, and VsEPs.

DPOAEs

DPOAE measures were completed for 8 C57BL/6J, 6 *Pls1*$^{+/+}$, 6 *Pls1*$^{+/-}$, 11 *Pls1*$^{-/-}$, 7 *Fscn2*$^{R109H/R109H}$, and 9 *Pls1*$^{-/-}$ *Fscn2*$^{R109H/R109H}$ mice. DPO AE stimuli were generated and controlled using TDT System III (RX6, PA5 modules) and SigGen/BioSig software. Pure tone frequencies (f2/f1 ratio = 1.25), at equal levels (L1 = L2 = 60 dB sound-pressure level [SPL]), 150 ms duration, were generated by RX6 multifunction processor, attenuated through PA5 programmable attenuators and routed

Published November 3, 2016

through separate drivers to mix acoustically in the ear canal via the same eartip used for ABR testing. Primary stimulus frequencies were such that the geometric mean (GM = $(f1 \times f2)^{0.5}$) frequencies ranged from 5.8 to 47.6 kHz. Ear canal SPLs were recorded with a low-noise probe microphone (ER 10B+; Etymotic Research Inc.). The microphone output was amplified 10 times and routed to the RX6 multifunction processor for sampling at 100 kHz and averaging of FFTs of the acoustic signals. The amplitudes of f1, f2, and the cubic (2f1-f2) distortion product were measured from the FFT waveform. The corresponding noise floor was determined from the mean sound levels in the fifth and tenth frequency bins above and below the 2f1-f2 frequency bin.

ABRs

ABR testing was completed for 8 C57BL/6, 6 *Pls1*$^{+/+}$, 6 *Pls1*$^{+/-}$, 11 *Pls1*$^{-/-}$, 7 *Fscn2*$^{R109H/R109H}$, and 10 *Pls1*$^{-/-}$ *Fscn2*$^{R109H/R109H}$ mice. For ABR testing, pure tone burst stimuli were generated and controlled using National Instruments data acquisition system and custom software. Tone bursts at 8, 16, 32, and 41.2 kHz had 1.0 ms rise and fall times with 1.0 ms plateau (3 ms total duration). Stimuli were calibrated using a Bruel and Kjaar 1/4-inch microphone and Nexus amplifier in decibel peak-equivalent SPL (Burkard, 2006) and were presented via high frequency transducers (SA1 speaker amplifier, MF1 speakers; Tucker-Davis Technologies) coupled at the ear via a modified commercial eartip (ER 10D-T03; Etymotic Research Inc.). Condensation and rarefaction tone bursts were presented at a rate of 17 stimuli per second. ABR intensity series were collected by initiating recordings at the maximum stimulus level and then reducing the stimulus in 5-dB steps until no response could be detected. Signal averaging was used to resolve ABR responses out of background electroencephalographic activity as described for VsEP recordings. For transient stimuli like those used for ABR, the SPL cannot be accurately measured with a sound level meter. Calibration therefore relied on measuring the decibel SPL of a long-duration tone with a peak-to-peak amplitude equivalent to the peak-to-peak amplitude of the transient stimulus, giving the peak-equivalent SPL.

VsEPs

VsEP measures were completed for 15 C57BL/6, 8 *Pls1*$^{+/+}$, 9 *Pls1*$^{+/-}$, 14 *Pls1*$^{-/-}$, 15 *Fscn2*$^{R109H/R109H}$, and 16 *Pls1*$^{-/-}$ *Fscn2*$^{R109H/R109H}$ mice. For VsEP testing, linear acceleration ramps (producing rectangular jerk pulses) were generated and controlled using National Instruments data acquisition system and custom software. Mice were placed supine on a stationary platform, and the head was secured within a spring clip coupled to a voltage-controlled mechanical shaker (Model 132-2; Labworks). The head was oriented with nose up, and linear translation stimuli were presented in the naso-occipital axis parallel to the earth-vertical axis. Vestibular stimuli consisted of 2-ms linear jerk pulses, delivered to the head using two stimulus polarities (normal, with an initial upward jerk, and inverted, with an initial downward jerk) at a rate of 17 pulses per second. Stimulus amplitudes ranged from +6 dB to −18 dB referenced to 1.0 *g*/ms (where 1 $g = 9.8$ m/s^2), adjusted in 3-dB steps. A broadband forward masker (50–50,000 Hz, 94 dB SPL) was presented during VsEP measurements to confirm the absence of auditory components (Jones and Jones, 1999).

Signal averaging was used to extract the VsEP responses from the background electrophysiological activity. Ongoing electroencephalographic activity was amplified (200,000×), filtered (300–3,000 Hz, −6 dB points), and digitized beginning at the onset of each jerk stimulus (1,024 points, 10 µs/point) to produce one primary response trace. For each stimulus intensity and polarity, 128 primary responses were averaged to produce an averaged response waveform. Four averaged response waveforms were recorded for each stimulus intensity (two waveforms recorded for normal stimulus polarity and two for inverted polarity). Final individual response traces were produced by summing one averaged response to each stimulus polarity and dividing the result by two, thus producing two response traces for each stimulus intensity for each animal.

Inner ear functional measure data analysis

Thresholds for VsEP (in dB referenced to 1.0 *g*/ms) and ABR (in dB peak-equivalent SPL) were defined as the stimulus level midway between the lowest level producing a discernible response and the maximum level where no response was observed. The first positive (p1) and negative (n1) response peaks of the VsEP and ABR waveforms were scored for latency (in milliseconds) and amplitude (in microvolts) at all stimulus levels. For DPOAEs, data points at 17.6, 20, and 21.2 kHz were excluded from the dataset, because these frequencies are at or near the ear canal standing wave resonances. For statistical comparisons, DPOAE absolute amplitudes for the remaining 2f1-f2 frequencies were averaged for each animal across low (6.4–26.2 kHz) and high (27.6–53.2 kHz) frequency ranges. A multivariate ANOVA analysis was used to compare thresholds, latencies, and amplitudes for differences among the genotypes. In cases where equality of error variance was not met (using Levine's test), Kruskal–Wallis independent samples nonparametric test was used with Dunn's pairwise comparisons. Significance level was set at 0.05 for all analyses.

Hair-bundle isolation

Hair bundles were isolated from P21 to P25 mouse utricles using the twist-off method, which is described in detail elsewhere (Gillespie and Hudspeth, 1991; Dumont et al., 2002; Krey et al., 2015). In brief, utricles were adhered to the bottom of a plastic tissue-culture disk, then were immersed in 4% agarose in Leibovitz-15 medium at 42°C. The agarose was cooled until firm, and then the utricles were yanked off, leaving the bundles in agarose. Damaged tissue imbedded in agarose was dissected away, and the recovery was estimated by examination using dark-field illumination and a dissecting microscope. Small blocks of agarose (<0.5 µl), each containing the bundles from a single ear, were dissected out and frozen at −80°C until use.

Isolation efficiency was examined using phalloidin staining of isolated bundles in agarose. Hair bundles were fixed for 20 min at room temperature in 4% formaldehyde (Electron Microscopy Sciences) in PBS. Agarose blocks were washed with PBS, permeabilized for 10 min in 0.5% Triton X-100 in PBS, and then incubated for 2 h at room temperature with Alexa Fluor 488 Phalloidin (1:500; Invitrogen) diluted in PBS. Agarose blocks were then rinsed three times for 10 min each, and then a thin disc containing the bundles was shaved from the block using a fine tungsten needle. Agarose sections were mounted on a slide using VECTASHIELD (Vector Laboratories). Images of isolated hair bundles were acquired at room temperature on a FluoView FV1000 laser scanning confocal microscope (Olympus) system and AF10-ASW 3.0 acquisition software, using a 10× 0.4 NA U Plan S-Apo objective with 1.5× zoom. Images were processed with Fiji (ImageJ) software. Brightness and contrast were globally adjusted and all z sections were merged into one plane using the Z project tool on Fiji.

Shotgun proteomics

We quantified stereocilia proteins from wild-type CD1 mice using shotgun MS with an Orbitrap mass spectrometer. Peptides were identified with Andromeda (Cox et al., 2011) and then quantified and assembled into proteins using MaxQuant (Cox and Mann, 2008). Technical details for these experiments have been reported previously (Krey et al., 2015), and the data are available from ProteomeXchange with the identifier PXD002167.

Published November 3, 2016

Comparative proteomics using *Pls1*$^{+/+}$ and *Pls1*$^{-/-}$ mice were performed using shotgun MS with an LTQ Velos ion-trap mass spectrometer. Peptides were identified with SEQUEST (Eng et al., 1994) and then assembled into proteins using the PAW pipeline (Wilmarth et al., 2009). Proteins were quantified using normalized molar intensity (Krey et al., 2014). The data are available from ProteomeXchange with the identifier PXD004044.

Targeted proteomics

For targeted MS/MS quantitation of cross-linkers, we measured ACT, PLS1, FSCN2, ESPN, and ESPN-1 peptides from four preparations of 10 ear equivalents of hair bundles isolated from P21 to P25 C57BL/6 mice and from four preparations from two different ages of CD-1 mice (P4–P6 and P21–P23), each of 13–14 ear equivalents of hair bundles. In-solution tryptic digests of the samples were prepared using an eFASP method (Erde et al., 2014). Proteins were digested in the filter unit in 100 µl digestion buffer with 200 ng sequencing-grade modified trypsin (Promega) at 37°C for 12–16 h. Three quantified synthetic stable-isotope–labeled peptides (SpikeTides-TQL) corresponding to each mouse protein sequence (ACT: EITALAPSTMK, GYSFTTTAER, AGFAGD DAPR; PLS1: IYALPDDLVEVKPK, MINLSEPDTIDER, VAFVNW INK; FSCN2: FFGGIEDR, FLVLPQPDGR, YLAPVGPAGTLK; ESPN: LAPWQR, LASLPAWR, TLGYDEAK; and ESPN-1: DNS GATVLHLAAR, YLVEEVALPAVSR, YLVQECSADPHLR) were obtained from JPT Peptide Technologies and used as internal standards; any cysteine residues were substituted by carbamoylmethylated cysteines during synthesis. The following amounts of each peptide were added along with the trypsin solution before digestion of each sample: ACT peptides, 500 fmol; PLS1 peptides, 50 fmol; FSCN2 peptides, 50 fmol; ESPN peptides 10 fmol; and ESPN1 peptides, 1 fmol. Calibration curves were run for all peptides by adding four dilutions of each peptide (centered on the amount spiked into the sample) to four mouse utricular lysate samples (0.5 ear equivalents) prepared in the same way as the bundle samples. Peptides were isolated by centrifugation and were extracted with ethyl acetate to remove remaining deoxycholic acid (Erde et al., 2014). Heavy and endogenous forms of each peptide were monitored by targeted MS/MS.

Peptide samples were analyzed with an Orbitrap Fusion Tribrid mass spectrometer (Thermo Fisher Scientific) coupled to a Thermo/Dionex Ultimate 3000 Rapid Separation UPLC system and EasySpray nanosource. Samples were loaded onto an Acclaim PepMap C18, 5-µm particle, 100-µm × 2-cm trap using a 5-µl/min flow rate and then separated on a EasySpray PepMap RSLC, C18, 2-µm particle, 75-µm × 25-cm column at a 300-nl/min flow rate. Solvent A was water, and solvent B was acetonitrile; each contained 0.1% (vol/vol) formic acid. After loading at 2% B for 5 min, peptides were separated using a 55-min gradient from 7.5–30% B, 10-min gradient from 30–90% B, and 6-min at 90% B, followed by a 19-min reequilibration at 2% B. Peptides were analyzed using the targeted MS2 mode of the Xcalibur software in which the doubly or triply charged precursor ion corresponding to each peptide was isolated in the quadrupole, fragmented by higher-energy collisional dissociation, and full *m/z* 350–1,600 scans of fragment ions at 30,000 resolution were collected in the Orbitrap. Targeted MS2 parameters included an isolation width of 2 *m/z* for each precursor of interest, collision energy of 30%, AGC target of 5×10^4, maximum ion injection time of 100 ms, spray voltage of 2,400 V, and ion transfer temperature of 275°C. No more than 75 precursors were targeted in each run, and no scheduling was used. Three unique peptides for each protein of interest were chosen for isolation based on previous data-dependent discovery data or from online peptide databases (http://www.peptideatlas.org and http://www.thegpm.org). Precursor isolation lists for all peptides of interest were exported from the software package Skyline (http://proteome.gs.washington.edu/software/skyline/) and imported into the Orbitrap control software.

Skyline was used to analyze targeted MS/MS data. Chromatographic and spectral data from the RAW files were loaded into Skyline and analyzed to determine fragment ion peaks corresponding to each peptide. RAW files were also processed using Proteome Discoverer (Thermo Fisher Scientific) software in order to match MS/MS spectra to an Ensembl spectral database using Sequest HT. Fragment ion peaks that coeluted with the fragment ion peaks for the corresponding heavy peptide were chosen for analysis. The type and proportion of daughter ions contributing to the peptide peak were required to match that of the heavy peptide peak. In addition, one or more spectra within the light or heavy peptide peak were matched to the correct peptide sequence within the spectral database. If spectra within a specific sample were not identified, then (a) the retention time of the chosen peak must be within 2 min of the retention time of an identified peak for that peptide from another sample, and (b) the type of daughter ions contributing to the peak must match the identified peptide peak from another sample. Chromatographic peak areas from all detected fragment ions for the light and heavy version of each peptide were integrated and summed, and then the peak area ratio between the light and heavy peptides was calculated. This ratio was multiplied by the amount of spiked heavy peptide to give the femtomole amount of each light peptide in the sample. The peptide femtomole amounts for each protein of interest were averaged for each sample (and normalized to the mean amount, in femtomoles, of actin within the same sample). The normalized peak areas were then averaged for the four biological replicates of each age and mouse strain to give a mean protein intensity measurement for each protein of interest. For the calibration curve samples, a linear regression of the heavy peptide peak area in each of the four calibration samples was performed and tested for linearity around the measurement range. Peptides that did not perform linearly ($R^2 > 0.98$) were excluded from analysis.

For targeted MS/MS experiments comparing relative protein expression in wild-type versus *Pls1*$^{-/-}$ bundles, peptides were measured from three (C57BL/6) or two (*Pls1*$^{-/-}$) preparations of 10 ear-equivalents of hair bundles. Peptides were generated using in-gel digestion methods, which have been previously described (Krey et al., 2015). Prior to digestion with trypsin, 150 fmol of heavy ACT peptides was added, and light peptide peak areas were measured for all other proteins of interest. Peptide peak areas for each protein were averaged for each sample and normalized to the mean peptide peak area for actin within the same sample. The normalized peak areas were then averaged for the three biological replicates of each genotype to give a mean protein intensity measurement for each protein of interest.

All targeted MS/MS data are available at https://panoramaweb.org/labkey/crosslinkers.url.

Immunoblotting

To each sample of mouse utricle hair bundles and whole utricles, NuPAGE 4× LDS sample buffer (NP0008; Thermo Fisher Scientific) and 10× reducing agent (NP0009; Thermo Fisher Scientific) were added to a final 1× concentration. Samples were heated at 65°C for 15 min and then at 95°C for 5 min, and resolved using 4–12% SDS-PAGE gels with MES or MOPS buffer (NuPAGE gels and buffers; Thermo Fisher Scientific). Proteins were transferred to PVDF (Immobilon-P; EMD Millipore) and were visualized with India Ink (1:5,000) in PBS/0.05% Tween-20. Membranes were blocked with Prime Blocking Agent (RPN418; GE Healthcare), and probed with specific primary antibodies which were detected with species-specific HRP-coupled secondary antibodies (AffiniPure 111-035-144 and 115-035-003; Jackson ImmunoResearch Laboratories, Inc.) and ECL Prime (RPN2232;

Published November 3, 2016

GE Healthcare). Intensity measurements were made using the Gel Analysis module on Fiji.

Immunocytochemistry

For direct immunostaining with cross-linker antibodies, dissected utricles (with otoconia removed) were fixed for 20 min at room temperature in 4% formaldehyde (Electron Microscopy Sciences) in PBS. Organs were rinsed in PBS, permeabilized for 10 min in 0.5% Triton X-100 in PBS, and blocked for 1 h in 5% normal donkey serum in PBS. Utricles were then incubated overnight at 4°C with fluorophore-labeled primary antibodies (see Antibodies section; 1:250 dilution) and either CF633 Phalloidin (1:500; Biotium) or Alexa Fluor 488 Phalloidin (1:1,000; Invitrogen), diluted in blocking solution. Tissue was then rinsed three times for 10 min each, postfixed in 4% formaldehyde for 5–10 min, and rinsed twice in PBS before mounting.

For stereocilia length analysis, ears were removed and holes were created in the bone near the vestibular organs. Ears were then incubated overnight at 4°C in 4% formaldehyde in PBS. After fixation, the utricles were dissected out in PBS, then incubated in 50 µg/ml protease XXVI (Sigma-Aldrich) in PBS for 5 min, and then otolithic membranes were removed with an eyelash. Organs were rinsed in PBS, permeabilized for 10 min in 0.5% Triton X-100 in PBS, and blocked for 1 h in 2% bovine serum albumin/5% normal donkey serum in PBS. Organs were incubated overnight at 4°C with anti-acetylated tubulin (T6793 clone 6-11B-1, 1:1,000; Sigma-Aldrich) diluted in blocking solution, and then rinsed three times for 10 min each. Organs were then incubated for 3–4 h in blocking solution with donkey anti–mouse IgG Alexa Fluor 647 (1:1,000; Invitrogen) secondary antibodies and 0.4 U/ml Alexa Fluor 488 Phalloidin (Molecular Probes and Invitrogen), followed by three 10-min rinses in PBS. All utricles were mounted on slides in VECTASHIELD using one Secure-Seal spacer (eight wells, 0.12 mm deep; Invitrogen).

For the isolated stereocilia samples used for SIM, utricles were dissected and otoconia were removed with an eyelash. Square #1.5 glass coverslips (Corning) were washed with water and 70% ethanol, autoclaved, and then coated with 100 µg/ml poly-L-lysine for 10–20 min. Poly-L-lysine was removed and coverslips dried for 30–60 min. Dissected utricles were dropped onto the coverslips in dissection media and gently pressed to the coverslip with the epithelium side down. The utricle and dissection solution was then removed and 200 µl of 4% formaldehyde (Electron Microscopy Sciences) in PBS was added to each coverslip for 20 min. Coverslips were rinsed three times with PBS and then placed on top of a Petri dish lid inside a humidity chamber. Samples were permeabilized for 15 min in 0.2% Triton X-100, 0.1% BSA, and 1% normal donkey serum in PBS and then blocked for 1 h in 0.1% bovine serum albumin/2% normal donkey serum in PBS. Coverslips were incubated overnight at 4°C with primary antibodies diluted in blocking solution and then rinsed three for 10 min each. Coverslips were then incubated for 3–4 h in blocking solution with Alexa Fluor 488 (1:1,000; Invitrogen) secondary antibodies (unless primary antibody was directly labeled) and CF633 Phalloidin (1:500; Biotium) followed by three 10-min rinses with PBS. Coverslips were rinsed briefly in water, excess water was blotted on a paper towel, and then coverslips were mounted on slides using EverBrite mounting medium (Biotium).

Confocal microscopy and image analysis

Utricle images were acquired at room temperature on a FluoView FV1000 laser scanning confocal microscope system (Olympus) and AF10-ASW 3.0 acquisition software, using a 60× 1.42 NA Plan-Apochromat objective with 4× zoom and 0.35-µm z-steps. All z-stacks were processed using Bitplane Imaris 7. 3D projections of each z-stack were visualized using the "Surpass" mode and were cropped along the x or y dimension to include one row of hair cells using the "Crop 3D" tool. The cropped 3D projection was then rotated in Surpass mode to visualize a y-z or x-z slab of the stack with the hair bundles oriented vertically, and the "Snapshot" tool was using to generate a tiff image of the projection. Stereocilia lengths were measured from the full z-stacks using the "Filaments" tool under manual mode in Bitplane Imaris 7. The lower and upper end of the longest stereocilium within each bundle was manually marked with a point within the 3D projection and then a filament connecting these points was automatically drawn and measured.

Isolated stereocilia images were acquired at room temperature using a 100× 1.46 NA Plan-Apochromat objective on a Elyra PS.1 system (ZEISS), which reconstructs superresolution images from a series of images acquired under SIM; the system uses an iXon 897 EMCCD camera (Andor Technology). Images were processed for SIM reconstruction in Zen 2012 (ZEISS), and selected Z-planes were exported as tiff images in Biplane Imaris 7. Stereocilia widths (at their widest dimension) were manually measured in slice mode in Bitplane Imaris 7 using the measurement tool.

Transmission EM: freeze-substitution protocol

Freeze substitution and immuno-gold labeling were performed as previously described (Rzadzinska et al., 2005; Francis et al., 2015). Utricles and organ of Corti were isolated from the inner ear, quickly transferred to 4% paraformaldehyde and 0.5% glutaraldehyde in phosphate buffer at pH 7.2, and allowed to fix for 2 h. The samples were slowly transitioned to 30% glycerol as a cryoprotectant and plunge-frozen in liquid ethane at −180°C using a Leica Biosystems grid plunger. Afterwards, the samples were freeze-substituted in a Leica Biosystems AFS with 1.5% uranyl acetate in absolute methanol at −90°C for 2 d and infiltrated with HM20 Lowicryl resin (Electron Microscopy Sciences) over the course of 2 d at −45°C. The resin was UV-polymerized for 3 d between −45°C and 0°C. Ultrathin sections were cut at 70 to 100 nm and collected on hexagonal 300-mesh Ni grids (Electron Microscopy Sciences). For immunogold labeling, sections were blocked with normal goat serum, incubated with rabbit anti-espin (PB127), and labeled with 10-nm colloidal gold conjugated to goat anti–rabbit secondary antibody. All freeze-substituted samples were imaged using a 200-kV JEOL 2100 of LaB6 gun type, which was equipped with a Gatan Orius 832 CCD camera. Acquisition software was DigitalMicrograph (Gatan); processing was done with DigitalMicrograph and Fiji and was limited to cropping and linear adjustments to brightness and contrast.

Transmission EM: dehydration protocol

Utricles from P21 to P25 mice were dissected in Leibovitz-15 and then immediately fixed for 0.3–1.5 h in 4% formaldehyde/1% glutaraldehyde (Ted Pella) in phosphate buffer at pH 7.2, followed by 40 min on ice in 1% glutaraldehyde/1% OsO_4 (Ted Pella) in 0.1 M phosphate buffer at pH 7.2. Fixed utricles were then thoroughly rinsed with H_2O. The tissues were stained en bloc in 0.5% uranyl acetate for 3 h at room temperature and then washed in H_2O. The utricles were subsequently dehydrated stepwise in acetone (50%, 75%, 95%, and 100%) at room temperature, using 10–15 min for each step. An overnight room-temperature incubation in 1:1 acetone/Araldite (Electron Microscopy Sciences) was performed, followed by embedding in freshly prepared Araldite in embedding molds (Ted Pella). Araldite was polymerized at 65°C for 48 h. Thick and thin sections were cut on an RMC Products MT-7000 ultramicrotome; thin sections were collected on 200-mesh, Rh-flashed copper Maxtaform grids (Ted Pella) and stained with Reynold's lead citrate and uranyl acetate. Sections were imaged on an 80-kV FEI Tecnai 12 BioTWIN transmission electron microscope with a tungsten filament gun, which was equipped with an AMT Active Vu-M 16 megapixel camera (Advanced Microscopy Techniques). Acquisition software was AMT

Image Capture Engine V602; processing was done with Fiji and was limited to cropping and linear adjustments to brightness and contrast.

Transmission EM: analysis

Fiji was used for analysis of transmission EM micrographs. Areas of interest in longitudinal or transverse sections of stereocilia were selected, and then the FFT tool was used to carry out a spatial Fourier transform on the selection. To measure cross-linker spacing from FFT transforms of transverse sections, for each stereocilium, three measurements were made from the image center to the spacing feature (ring or hexagon), which were averaged together; the inverse of this distance equals the cross-linker spacing (read out directly in Fiji, however). Approximately 100 measurements were made for each genotype.

Fourier filtering was performed with DigitalMicrograph and Fiji. The area to be filtered was selected and then FFT-transformed. A hexagonal mask was placed over the predominant reflections in Fourier space using the masking tools built-in DigitalMicrograph, making the mask as tight as possible to reduce background Fourier signal. After applying the mask, an inverse FFT was taken to generate the corresponding real-space image; this image was thresholded in Fiji to remove any background signal and then added back to the original.

Online supplemental material

Fig. S1 is a characterization of stereocilia in *Pls1*$^{-/-}$ mice. Fig. S2 shows latencies and amplitudes for ABRs at 8 kHz. Fig. S3 shows latencies and amplitudes for vestibular evoked potentials. Fig. S4 shows a quantitation of PLS1 and FSCN2 in whole epithelium by quantitative immunoblotting and MS. Fig. S5 is a comparison of hair-bundle proteins after in-gel digest or direct digestion.

Acknowledgments

We thank Ruby Larisch for mouse husbandry support and Runjia Cui for technical help, as well as Ben Perrin and Stefan Heller for antibodies.

The work described here was supported by National Institutes of Health grants R01 DC002368 (P.G. Barr-Gillespie), R01 DC011034 (P.G. Barr-Gillespie), P30 DC005983 (P.G. Barr-Gillespie), and F32 DC012455 (J.F. Krey). E.S. Krystofiak and B. Kachar were supported by the National Institute on Deafness and Other Communication Disorders Intramural Research Program (Z01 DC000002). S.M. Jones was supported by the Nebraska Tobacco Settlement Biomedical Research Development Fund. We received support from the following core facilities: shotgun and targeted MS from the Oregon Health and Science University (OHSU) Proteomics Shared Resource, confocal and SIM from the OHSU Advanced Light Microscopy Core at The Jungers Center, EM from the OHSU Multiscale Microscopy Core, and EM from the National Institute on Deafness and Other Communication Disorders Advanced Imaging Core (ZIC DC000081).

The authors declare no competing financial interests.

Submitted: 6 June 2016
Revised: 29 September 2016
Accepted: 11 October 2016

References

Avenarius, M.R., K.W. Saylor, M.R. Lundeberg, P.A. Wilmarth, J.B. Shin, K.J. Spinelli, J.M. Pagana, L. Andrade, B. Kachar, D. Choi, et al. 2014. Correlation of actin crosslinker and capper expression levels with stereocilia growth phases. *Mol. Cell. Proteomics.* 13:606–620. http://dx.doi.org/10.1074/mcp.M113.033704

Burkard, R. 2006. Calibration of acoustic transients. *Brain Res.* 1091:27–31. http://dx.doi.org/10.1016/j.brainres.2006.02.132

Chhabra, E.S., and H.N. Higgs. 2007. The many faces of actin: matching assembly factors with cellular structures. *Nat. Cell Biol.* 9:1110–1121. http://dx.doi.org/10.1038/ncb1007-1110

Claessens, M.M., C. Semmrich, L. Ramos, and A.R. Bausch. 2008. Helical twist controls the thickness of F-actin bundles. *Proc. Natl. Acad. Sci. USA.* 105:8819–8822. http://dx.doi.org/10.1073/pnas.0711149105

Cox, J., and M. Mann. 2008. MaxQuant enables high peptide identification rates, individualized p.p.b.-range mass accuracies and proteome-wide protein quantification. *Nat. Biotechnol.* 26:1367–1372. http://dx.doi.org/10.1038/nbt.1511

Cox, J., N. Neuhauser, A. Michalski, R.A. Scheltema, J.V. Olsen, and M. Mann. 2011. Andromeda: a peptide search engine integrated into the MaxQuant environment. *J. Proteome Res.* 10:1794–1805. http://dx.doi.org/10.1021/pr101065j

Crawley, S.W., M.S. Mooseker, and M.J. Tyska. 2014. Shaping the intestinal brush border. *J. Cell Biol.* 207:441–451. http://dx.doi.org/10.1083/jcb.201407015

DeRosier, D.J., and P.B. Moore. 1970. Reconstruction of three-dimensional images from electron micrographs of structures with helical symmetry. *J. Mol. Biol.* 52:355–369. http://dx.doi.org/10.1016/0022-2836(70)90036-7

DeRosier, D.J., and L.G. Tilney. 1982. How actin filaments pack into bundles. *Cold Spring Harb. Symp. Quant. Biol.* 46:525–540. http://dx.doi.org/10.1101/SQB.1982.046.01.049

DeRosier, D.J., and L.G. Tilney. 1984. The form and function of actin. A product of its unique design. *Cell Muscle Motil.* 5:139–169.

DeRosier, D.J., L.G. Tilney, and E. Egelman. 1980. Actin in the inner ear: the remarkable structure of the stereocilium. *Nature.* 287:291–296. http://dx.doi.org/10.1038/287291a0

Drummond, M.C., I.A. Belyantseva, K.H. Friderici, and T.B. Friedman. 2012. Actin in hair cells and hearing loss. *Hear. Res.* 288:89–99. http://dx.doi.org/10.1016/j.heares.2011.12.003

Dumont, R.A., Y.D. Zhao, J.R. Holt, M. Bähler, and P.G. Gillespie. 2002. Myosin-I isozymes in neonatal rodent auditory and vestibular epithelia. *J. Assoc. Res. Otolaryngol.* 3:375–389. http://dx.doi.org/10.1007/s101620020049

Ebrahim, S., M.R. Avenarius, M. Grati, J.F. Krey, A.M. Windsor, A.D. Sousa, A. Ballesteros, R. Cui, B.A. Millis, F.T. Salles, et al. 2016. Stereocilia-staircase spacing is influenced by myosin III motors and their cargos espin-1 and espin-like. *Nat. Commun.* 7:10833. http://dx.doi.org/10.1038/ncomms10833

Egelman, E.H., N. Francis, and D.J. DeRosier. 1982. F-actin is a helix with a random variable twist. *Nature.* 298:131–135. http://dx.doi.org/10.1038/298131a0

Eng, J.K., A.L. McCormack, and J.R. Yates. 1994. An approach to correlate tandem mass spectral data of peptides with amino acid sequences in a protein database. *J. Am. Soc. Mass Spectrom.* 5:976–989. http://dx.doi.org/10.1016/1044-0305(94)80016-2

Erde, J., R.R. Loo, and J.A. Loo. 2014. Enhanced FASP (eFASP) to increase proteome coverage and sample recovery for quantitative proteomic experiments. *J. Proteome Res.* 13:1885–1895. http://dx.doi.org/10.1021/pr4010019

Francis, S.P., J.F. Krey, E.S. Krystofiak, R. Cui, S. Nanda, W. Xu, B. Kachar, P.G. Barr-Gillespie, and J.B. Shin. 2015. A short splice form of Xin-actin binding repeat containing 2 (XIRP2) lacking the Xin repeats is required for maintenance of stereocilia morphology and hearing function. *J. Neurosci.* 35:1999–2014. http://dx.doi.org/10.1523/JNEUROSCI.3449-14.2015

Gallien, S., and B. Domon. 2015. Advances in high-resolution quantitative proteomics: implications for clinical applications. *Expert Rev. Proteomics.* 12:489–498. http://dx.doi.org/10.1586/14789450.2015.1069188

Gardel, M.L., J.H. Shin, F.C. MacKintosh, L. Mahadevan, P. Matsudaira, and D.A. Weitz. 2004. Elastic behavior of cross-linked and bundled actin networks. *Science.* 304:1301–1305. http://dx.doi.org/10.1126/science.1095087

Gillespie, P.G., and A.J. Hudspeth. 1991. High-purity isolation of bullfrog hair bundles and subcellular and topological localization of constituent proteins. *J. Cell Biol.* 112:625–640. http://dx.doi.org/10.1083/jcb.112.4.625

Grimm-Günter, E.M., C. Revenu, S. Ramos, I. Hurbain, N. Smyth, E. Ferrary, D. Louvard, S. Robine, and F. Rivero. 2009. Plastin 1 binds to keratin and is required for terminal web assembly in the intestinal epithelium. *Mol. Biol. Cell.* 20:2549–2562. http://dx.doi.org/10.1091/mbc.E08-10-1030

Grüneberg, H., J.B. Burnett, and G.D. Snell. 1941. The origin of Jerker, a new gene mutation of the house mouse, and linkage studies made with it. *Proc. Natl. Acad. Sci. USA.* 27:562–565. http://dx.doi.org/10.1073/pnas.27.12.562

Gupton, S.L., and F.B. Gertler. 2007. Filopodia: the fingers that do the walking. *Sci. STKE.* 2007:re5. http://dx.doi.org/10.1126/stke.4002007re5

Gustafsson, M.G. 2000. Surpassing the lateral resolution limit by a factor of two using structured illumination microscopy. *J. Microsc.* 198:82–87. http://dx.doi.org/10.1046/j.1365-2818.2000.00710.x

Hudspeth, A.J. 1989. How the ear's works work. *Nature.* 341:397–404. http://dx.doi.org/10.1038/341397a0

Hwang, P., S.W. Chou, Z. Chen, and B.M. McDermott Jr. 2015. The stereociliary paracrystal Is a dynamic cytoskeletal scaffold in vivo. *Cell Reports.* 13:1287–1294. http://dx.doi.org/10.1016/j.celrep.2015.10.003

Jansen, S., A. Collins, C. Yang, G. Rebowski, T. Svitkina, and R. Dominguez. 2011. Mechanism of actin filament bundling by fascin. *J. Biol. Chem.* 286:30087–30096. http://dx.doi.org/10.1074/jbc.M111.251439

Jones, T.A., and S.M. Jones. 1999. Short latency compound action potentials from mammalian gravity receptor organs. *Hear. Res.* 136:75–85. http://dx.doi.org/10.1016/S0378-5955(99)00110-0

Jones, S.M., K.R. Johnson, H. Yu, L.C. Erway, K.N. Alagramam, N. Pollak, and T.A. Jones. 2005. A quantitative survey of gravity receptor function in mutant mouse strains. *J. Assoc. Res. Otolaryngol.* 6:297–310. http://dx.doi.org/10.1007/s10162-005-0009-4

Jones, S.M., T.A. Jones, K.R. Johnson, H. Yu, L.C. Erway, and Q.Y. Zheng. 2006. A comparison of vestibular and auditory phenotypes in inbred mouse strains. *Brain Res.* 1091:40–46. http://dx.doi.org/10.1016/j.brainres.2006.01.066

Krey, J.F., P.A. Wilmarth, J.B. Shin, J. Klimek, N.E. Sherman, E.D. Jeffery, D. Choi, L.L. David, and P.G. Barr-Gillespie. 2014. Accurate label-free protein quantitation with high- and low-resolution mass spectrometers. *J. Proteome Res.* 13:1034–1044. http://dx.doi.org/10.1021/pr401017h

Krey, J.F., N.E. Sherman, E.D. Jeffery, D. Choi, and P.G. Barr-Gillespie. 2015. The proteome of mouse vestibular hair bundles over development. *Sci. Data.* 2:150047. http://dx.doi.org/10.1038/sdata.2015.47

Li, A., J. Xue, and E.H. Peterson. 2008. Architecture of the mouse utricle: macular organization and hair bundle heights. *J. Neurophysiol.* 99:718–733. http://dx.doi.org/10.1152/jn.00831.2007

Merritt, R.C., U. Manor, F.T. Salles, M. Grati, A.C. Dose, W.C. Unrath, O.A. Quintero, C.M. Yengo, and B. Kachar. 2012. Myosin IIIB uses an actin-binding motif in its espin-1 cargo to reach the tips of actin protrusions. *Curr. Biol.* 22:320–325. http://dx.doi.org/10.1016/j.cub.2011.12.053

Michelot, A., and D.G. Drubin. 2011. Building distinct actin filament networks in a common cytoplasm. *Curr. Biol.* 21:R560–R569. http://dx.doi.org/10.1016/j.cub.2011.06.019

Mogensen, M.M., A. Rzadzinska, and K.P. Steel. 2007. The deaf mouse mutant whirler suggests a role for whirlin in actin filament dynamics and stereocilia development. *Cell Motil. Cytoskeleton.* 64:496–508. http://dx.doi.org/10.1002/cm.20199

Perrin, B.J., K.J. Sonnemann, and J.M. Ervasti. 2010. β-actin and γ-actin are each dispensable for auditory hair cell development but required for stereocilia maintenance. *PLoS Genet.* 6:e1001158. http://dx.doi.org/10.1371/journal.pgen.1001158

Perrin, B.J., D.M. Strandjord, P. Narayanan, D.M. Henderson, K.R. Johnson, and J.M. Ervasti. 2013. β-Actin and fascin-2 cooperate to maintain stereocilia length. *J. Neurosci.* 33:8114–8121. http://dx.doi.org/10.1523/JNEUROSCI.0238-13.2013

Purdy, K.R., J.R. Bartles, and G.C. Wong. 2007. Structural polymorphism of the actin-espin system: a prototypical system of filaments and linkers in stereocilia. *Phys. Rev. Lett.* 98:058105. http://dx.doi.org/10.1103/PhysRevLett.98.058105

Revenu, C., F. Ubelmann, I. Hurbain, F. El-Marjou, F. Dingli, D. Loew, D. Delacour, J. Gilet, E. Brot-Laroche, F. Rivero, et al. 2012. A new role for the architecture of microvillar actin bundles in apical retention of membrane proteins. *Mol. Biol. Cell.* 23:324–336. http://dx.doi.org/10.1091/mbc.E11-09-0765

Rzadzinska, A., M. Schneider, K. Noben-Trauth, J.R. Bartles, and B. Kachar. 2005. Balanced levels of Espin are critical for stereociliary growth and length maintenance. *Cell Motil. Cytoskeleton.* 62:157–165. http://dx.doi.org/10.1002/cm.20094

Salles, F.T., R.C.J. Merritt Jr., U. Manor, G.W. Dougherty, A.D. Sousa, J.E. Moore, C.M. Yengo, A.C. Dosé, and B. Kachar. 2009. Myosin IIIa boosts elongation of stereocilia by transporting espin 1 to the plus ends of actin filaments. *Nat. Cell Biol.* 11:443–450. http://dx.doi.org/10.1038/ncb1851

Sekerková, G., C.P. Richter, and J.R. Bartles. 2011. Roles of the espin actin-bundling proteins in the morphogenesis and stabilization of hair cell stereocilia revealed in CBA/CaJ congenic jerker mice. *PLoS Genet.* 7:e1002032. http://dx.doi.org/10.1371/journal.pgen.1002032

Shepherd, G.M.G., D.P. Corey, and S.M. Block. 1990. Actin cores of hair-cell stereocilia support myosin motility. *Proc. Natl. Acad. Sci. USA.* 87:8627–8631. http://dx.doi.org/10.1073/pnas.87.21.8627

Shevchenko, A., H. Tomas, J. Havlis, J.V. Olsen, and M. Mann. 2006. In-gel digestion for mass spectrometric characterization of proteins and proteomes. *Nat. Protoc.* 1:2856–2860. http://dx.doi.org/10.1038/nprot.2006.468

Shin, H., K.R. Purdy Drew, J.R. Bartles, G.C. Wong, and G.M. Grason. 2009. Cooperativity and frustration in protein-mediated parallel actin bundles. *Phys. Rev. Lett.* 103:238102. http://dx.doi.org/10.1103/PhysRevLett.103.238102

Shin, J.B., C.M. Longo-Guess, L.H. Gagnon, K.W. Saylor, R.A. Dumont, K.J. Spinelli, J.M. Pagana, P.A. Wilmarth, L.L. David, P.G. Gillespie, and K.R. Johnson. 2010. The R109H variant of fascin-2, a developmentally regulated actin crosslinker in hair-cell stereocilia, underlies early-onset hearing loss of DBA/2J mice. *J. Neurosci.* 30:9683–9694. http://dx.doi.org/10.1523/JNEUROSCI.1541-10.2010

Shin, J.B., J.F. Krey, A. Hassan, Z. Metlagel, A.N. Tauscher, J.M. Pagana, N.E. Sherman, E.D. Jeffery, K.J. Spinelli, H. Zhao, et al. 2013. Molecular architecture of the chick vestibular hair bundle. *Nat. Neurosci.* 16:365–374. http://dx.doi.org/10.1038/nn.3312

Taylor, R., A. Bullen, S.L. Johnson, E.M. Grimm-Günter, F. Rivero, W. Marcotti, A. Forge, and N. Daudet. 2015. Absence of plastin 1 causes abnormal maintenance of hair cell stereocilia and a moderate form of hearing loss in mice. *Hum. Mol. Genet.* 24:37–49. http://dx.doi.org/10.1093/hmg/ddu417

Tilney, L.G., and D.J. DeRosier. 1986. Actin filaments, stereocilia, and hair cells of the bird cochlea. IV. How the actin filaments become organized in developing stereocilia and in the cuticular plate. *Dev. Biol.* 116:119–129. http://dx.doi.org/10.1016/0012-1606(86)90048-5

Tilney, L.G., and M.S. Tilney. 1988. The actin filament content of hair cells of the bird cochlea is nearly constant even though the length, width, and number of stereocilia vary depending on the hair cell location. *J. Cell Biol.* 107:2563–2574. http://dx.doi.org/10.1083/jcb.107.6.2563

Tilney, L.G., D.J. Derosier, and M.J. Mulroy. 1980. The organization of actin filaments in the stereocilia of cochlear hair cells. *J. Cell Biol.* 86:244–259. http://dx.doi.org/10.1083/jcb.86.1.244

Tilney, L.G., E.H. Egelman, D.J. DeRosier, and J.C. Saunder. 1983. Actin filaments, stereocilia, and hair cells of the bird cochlea. II. Packing of actin filaments in the stereocilia and in the cuticular plate and what happens to the organization when the stereocilia are bent. *J. Cell Biol.* 96:822–834. http://dx.doi.org/10.1083/jcb.96.3.822

Tilney, M.S., L.G. Tilney, R.E. Stephens, C. Merte, D. Drenckhahn, D.A. Cotanche, and A. Bretscher. 1989. Preliminary biochemical characterization of the stereocilia and cuticular plate of hair cells of the chick cochlea. *J. Cell Biol.* 109:1711–1723. http://dx.doi.org/10.1083/jcb.109.4.1711

Vignjevic, D., S. Kojima, Y. Aratyn, O. Danciu, T. Svitkina, and G.G. Borisy. 2006. Role of fascin in filopodial protrusion. *J. Cell Biol.* 174:863–875. http://dx.doi.org/10.1083/jcb.200603013

Volkmann, N., D. DeRosier, P. Matsudaira, and D. Hanein. 2001. An atomic model of actin filaments cross-linked by fimbrin and its implications for bundle assembly and function. *J. Cell Biol.* 153:947–956. http://dx.doi.org/10.1083/jcb.153.5.947

Waingeh, V.F., C.D. Gustafson, E.I. Kozliak, S.L. Lowe, H.R. Knull, and K.A. Thomasson. 2006. Glycolytic enzyme interactions with yeast and skeletal muscle F-actin. *Biophys. J.* 90:1371–1384. http://dx.doi.org/10.1529/biophysj.105.070052

Wilmarth, P.A., M.A. Riviere, and L.L. David. 2009. Techniques for accurate protein identification in shotgun proteomic studies of human, mouse, bovine, and chicken lenses. *J. Ocul. Biol. Dis. Infor.* 2:223–234. http://dx.doi.org/10.1007/s12177-009-9042-6

Zheng, L., G. Sekerková, K. Vranich, L.G. Tilney, E. Mugnaini, and J.R. Bartles. 2000. The deaf jerker mouse has a mutation in the gene encoding the espin actin-bundling proteins of hair cell stereocilia and lacks espins. *Cell.* 102:377–385. http://dx.doi.org/10.1016/S0092-8674(00)00042-8